ELEMENTA
Science of the Anthropocene

Tao, R, et al. 2025. Spatial variability in surface brightness and solar energy deposition of Arctic sea ice. *Elem Sci Anth*, 13: 1.
DOI: https://doi.org/10.1525/elementa.2024.00084

RESEARCH ARTICLE

Spatial variability in surface brightness and solar energy deposition of Arctic sea ice

Ran Tao[1,2,*], Marcel Nicolaus[1], Christian Katlein[1], Niels Fuchs[3], Niklas Neckel[1], Lena Buth[1,2], Madison M. Smith[4], Bonnie Light[5], Steffen Graupner[1], and Christian Haas[1,2]

Sea ice modulates the transfer of shortwave radiative energy fluxes within the Arctic atmosphere-sea-ice-ocean system. Understanding and predicting these fluxes comes with greatest uncertainties during the melt and freeze-up seasons, when the sea ice surface is strongly heterogeneous and changing rapidly. Then, the partitioning of solar radiative fluxes between atmosphere, ice, and ocean has greatest impacts on the surface energy budget, controlling sea ice melt and formation. Here, we investigated changes and impacts of sea ice surface variability by analyzing high-resolution red-green-blue aerial imagery obtained during the Multidisciplinary Observatory for the Study of Arctic Climate (MOSAiC) expedition in 2020. We used pixel brightness from processed aerial images as a proxy of surface albedo, because such data are frequently available and obtainable from commercial digital cameras. The results allowed quantification of fluxes on floe-scales and also revealed the seasonality of sea ice spatial heterogeneity, which was strongest in the middle of melt season driven by melt pond processes. On scales of 10 m × 10 m, a magnitude larger than the traditional single in-situ optical observations (although many are made over larger scales), distinct surface conditions, for example, individual melt ponds, resulted in differences of energy deposition into the ice by more than 600%. The effects of spatial variability were minimized by integrating over areas 200 m × 200 m and larger. We suggest considering these scales for future energy budget studies and airborne observations, because sufficient parts of different surface features are included. The concept of surface brightness and aerial photographs might help to bridge in-situ observations to even larger scales, including fractions of open water. It may also be used to upscale observations of under-ice light regimes by providing spatially continuous surface brightness that governs the light transmittance, thus to improve our understanding of the coupled system, including ecological functions.

Keywords: Arctic sea ice, Sea ice albedo, Sea ice upscaling, Radiative fluxes

1. Introduction

Arctic sea ice modulates the transfer of radiative energy fluxes within the atmosphere-sea-ice-ocean system (Perovich, 2005; Hudson et al., 2013; Boeke and Taylor, 2018). In the warming Arctic, sea ice experiences an earlier melt onset and a more rapid ice loss in summer compared to historical norms, thus a longer melt season and higher radiative energy deposition (Perovich et al., 2002; Nicolaus et al., 2010; Perovich and Polashenski, 2012; Serreze and Stroeve, 2015; Stroeve and Notz, 2018). The excessive solar radiative energy deposited into the Arctic system triggers the ice albedo feedback (Grenfell and Maykut, 1977; Perovich, 1996; Kashiwase et al., 2017). In autumn and winter, near-surface air temperatures are enhanced as the ocean releases heat that was previously deposited mainly via leads or open water, but also through the ice and snow cover during summer (Kashiwase et al., 2017), the so-called indirect surface albedo effect (Wendisch et al., 2019).

After melt onset in spring, the sea ice surface albedo decreases and the radiative energy deposition increases (Curry et al., 1995; Bliss and Anderson, 2018). Virtually all the radiative energy is deposited during the sunlit months from May to September, with 96% of the annual solar heat input through sea ice occurring during the 4-month period from May to August. In addition, sea ice surface types become more variable (e.g., bare ice, melt pond, leads, etc.), increasing the spatial variability. Particularly during the spring–summer transition, when the

---

[1] Alfred-Wegener-Institut Helmholtz-Zentrum für Polar- und Meeresforschung, Bremerhaven, Germany

[2] Institute of Environmental Physics, University of Bremen, Bremen, Germany

[3] Center for Earth System Sustainability, Institute of Oceanography, University of Hamburg, Hamburg, Germany

[4] Woods Hole Oceanographic Institution, Woods Hole, MA, USA

[5] Polar Science Center, Applied Physics Laboratory, University of Washington, Seattle, WA, USA

[*] Corresponding author:
Email: ran.tao@awi.de

incident irradiance peaks, understanding the sea ice surface spatial variability is important to understand the sea ice radiative energy budget. Melt ponds can reduce sea ice albedo significantly; for instance, a ponding event can decrease the broadband albedo from 0.73 to 0.44, increasing the daily surface energy influx to nearly twice the preponding phase (Tao et al., 2024). Light et al. (2022) found that numerical models need most improvement in the spring–summer transition, to better describe surface albedo and energy fluxes. A main deficit is the huge uncertainty resulting from the increasing spatial variability of surface conditions and their non-linear seasonal evolution (Tao et al., 2024).

Therefore, investigating the impact of sea ice surface variability on radiative energy deposition during summer, from surface melt onset to freeze-up, is important. During summer, the sea ice surface undergoes significant changes in both brightness and energy deposition, driven by evolving melt and refreeze processes. These periods are marked by highly variable surface conditions, where melt ponds, bare ice, and refrozen areas coexist, contributing to fluctuations in surface albedo and the partitioning of solar energy. As melt ponds develop in early summer, the sea ice albedo decreases, intensifying energy deposition. By late summer, the onset of refreezing leads to an increase in surface brightness, which reduces the total energy deposition. This dynamic interplay between surface types, albedo, and solar irradiance during the transitional seasons is critical for understanding the Arctic sea ice energy budget. Accurate characterization of these surface changes is especially important, as the timing and extent of melt pond formation and refreezing directly influence the feedback mechanisms governing sea ice melt and growth.

There are many means to investigate the changes in sea ice surface albedo, spanning from handheld measurements along fixed lines (e.g., Perovich et al., 2002; Light et al., 2022) to autonomous radiation stations (e.g., Nicolaus et al., 2010; Tao et al., 2024), aerial imagery, and satellite remote sensing. Airborne imagery has been a powerful tool to investigate and classify the changes in the sea ice surface over areas at kilometer scales. During the Surface Heat Budget of the Arctic Ocean expedition (SHEBA, 1997–1998), Tschudi et al. (2001) used video camera imagery to investigate the changes in melt pond fraction (MPF) over a 20 km × 20 km area. Aerial imagery indicated that the maximum MPF occurred after mid-July, which was earlier than reported by Perovich et al. (1999) based on surface measurements over a 200 m-long line. A decade later, Sankelo et al. (2010) also monitored the rapidly increasing MPF when transitioning into summer during the Tara drift in the central Arctic. More recently, with the advanced development of digital cameras, airborne-based red-green-blue (RGB) imagery has been used frequently to assess changes in sea ice surface properties, such as brightness and classification (e.g., Renner et al., 2013; Katlein et al., 2015, Wang et al., 2018; Fuchs, 2023). Katlein et al. (2015) calculated the brightness of the sea ice surface within the visible wavelength range as the mean of the three color components divided by the total intensity of 255. The approach of using simple RGB imagery of the sea ice surface provides a straightforward way to evaluate the spatial variability of the sea ice surface. Its high-resolution aerial images span from decimeter to kilometer scales, thus linking the meter-scale observation to sub-satellite grid scale.

Here, we investigated the seasonal changes in sea ice surface variability and their impacts on radiative fluxes during the transitional seasons of the Arctic, demonstrating how a simple approach may be applied to investigate the scales of spatial variability of an ice floe. We used surface brightness from aerial imagery taken via helicopter and drone flights as a proxy for surface albedo. Based on the dataset from the Multidisciplinary Observatory for the Study of Arctic Climate (MOSAiC) expedition (Nicolaus et al., 2022), we quantified the energy deposition across different spatial and temporal scales to contribute to a more comprehensive understanding of sea ice energy budgets. This study also provides guidance for future expeditions and fieldwork, highlighting an approach to the minimum ground survey area necessary to ensure and to derive the upscaling of surface representativeness of different sea ice conditions.

2. Methods

2.1. The MOSAiC expedition and study sites

The dataset presented in this study was obtained as part of the MOSAiC expedition with the German ice-breaking research vessel (RV) *Polarstern* (Knust, 2017; Nicolaus et al., 2022; Shupe et al., 2022). We focused on the advanced melting phase and the freezing-up period, in June–July and August–September, respectively, which were the Drift 2 and Drift 3 of the MOSAiC expedition (Nicolaus et al., 2022; Tao et al., 2024). The sea ice surface conditions during advanced melting phase and the freeze-up are shown in **Figure 1**.

Drift 2 started on June 19 and ended on July 31, 2020, drifting southward toward Fram Strait to 78.9°N. Drift 2 was characterized by the peak incident irradiance and sea ice variability (Light et al., 2022; Webster et al., 2022; Tao et al., 2024). Drift 3 took place in the central Arctic (87.7°N) from August 21 to September 20, 2020. During this period, the air temperature showed a rapid decrease and the incident irradiance was an order of magnitude smaller than the melting season (Drift 2). More detailed meteorological conditions are described in Shupe et al. (2022) and Cox et al. (2023).

2.2. Acquisition of aerial images

Sea ice surface imagery was taken during helicopter and drone flights (e.g., **Figure 1**), covering various surface types ranging from melt ponds, bare ice, and snow-covered sea ice. The helicopter images were acquired with a nadir-looking CANON EOS-1D Mark III commercially available digital camera with a 14 mm lens, which provides wide field and relatively distortion-free optics (Ehrlich et al., 2012; Carlsen et al., 2020; Fuchs, 2023). The maxima of the RGB color band sensitivity of the camera are located at wavelengths of 600 nm (red, R), 545 nm (green, G), and 477 nm (blue, B), spanning the wavelength range from 400 nm to 700 nm (Fuchs, 2023). The

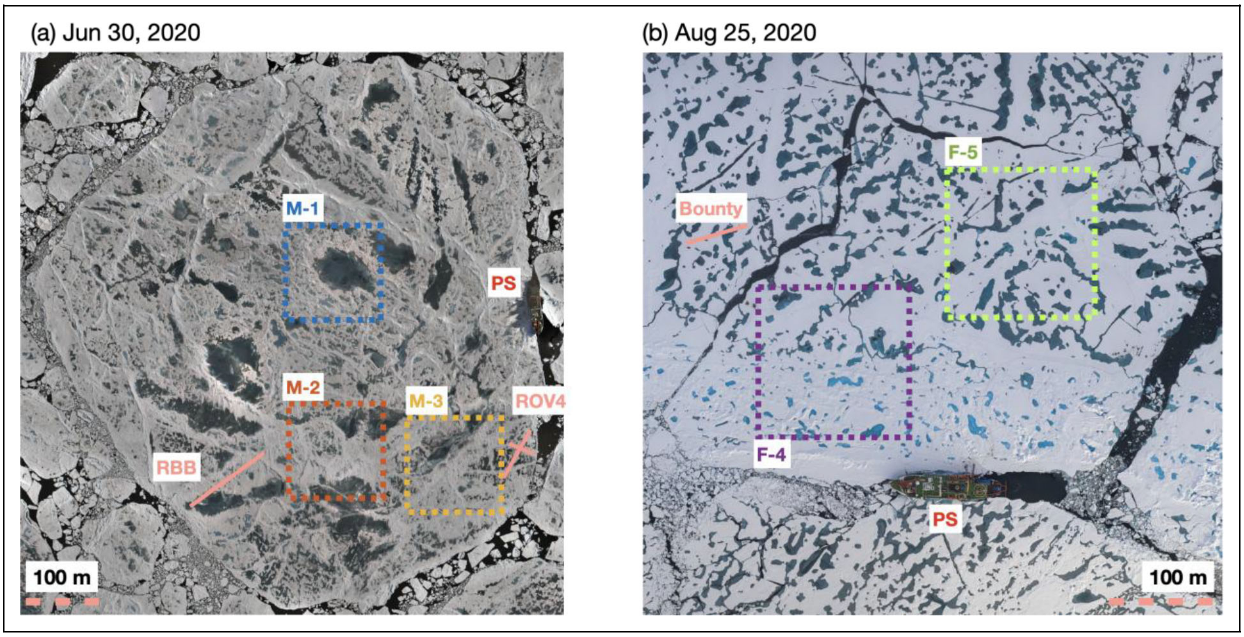

Figure 1. Aerial photos of the sea ice surface with focus areas and in-situ albedo line observation. All focus areas have a size of 200 m × 200 m. (a) June 30, 2020, at Central Observatory 2, with areas M-1 (blue), M-2 (orange), and M-3 (gold) indicated by dotted lines. Solid pink lines show the albedo lines, designated ROV4 (for remotely operated vehicle 4) and RBB (for root beer barrel). (b) August 25, 2020, at Central Observatory 3 with areas F-4 (dotted purple lines) and F-5 (dotted green lines), and albedo line Bounty. The position of RV *Polarstern* is indicated with PS.

sensitivity in all color bands to brightness changes was fully linear (Fuchs, 2023). The aerial images were taken at a frequency of 0.25 Hz at an average flight speed of approximately 42 m s^{-1} and altitude above 300 m during regular flight grids over the Central Observatory (Neckel et al., 2023). Collected raw images were converted to tagged image file format (TIFF) with flight-specific brightness corrections. Then, each image was assigned with the in-flight GNSS (latitude, longitude, altitude) and the inertial navigation system (roll, pitch, yaw) measurements (Neckel et al., 2023). Direct georeferencing was used to remove distortion (Fuchs, 2023). The mean sea ice drift velocity during the MOSAiC expedition was 0.098 m s^{-1} (Krumpen et al., 2021), which resulted in an average sea-ice displacement of approximately 700 m during a 2-h flight (Neckel et al., 2023). The sea ice drift was corrected from the difference between the position of RV *Polarstern* and a reference point at the center time of the flight (Neckel et al., 2023). Orthomosaics were created using Agisoft Metashape at a full spatial resolution, which varied between 0.03 m and 0.50 m (Neckel et al., 2023). A detailed description of the helicopter-borne aerial photographs can be found in Neckel et al. (2023).

Drone images were taken with a Mavic 3 (DJI) drone with a Hasselblad camera with 5280 × 3956 pixels, a focal length of 24 mm, and an opening angle of 84°. Flights were performed at a fixed altitude of 250 m, resulting in a horizontal resolution of 0.05 m per pixel. The drone was positioned manually with an overlap from image to image of approximately 30% to cover the target area. Exposure time, aperture, and ISO were set constant for each grid flight, based on one reference photo in automatic mode at the beginning of each flight. Collected raw images were converted to jpg format and stitched using PT-GUI software.

The stitched image (orthomosaics) was re-sampled to 0.5 m resolution per pixel to match the resolution of the other data products and enable comparison to surface albedo measurements. We rotated the aerial orthomosaics with known features (e.g., traces of in-situ measurement lines, RV *Polarstern*) to a fixed field of view of the ice floe.

2.3. Deriving surface brightness from aerial imagery

The orthomosaics of the sea ice and snow surface consisted of RGB channels. The digital intensity of each channel ranged from 0 to 255. The surface brightness was derived from the mean of the RGB intensity divided by 255. The surface brightness of the sea ice was then scaled linearly between 0.85 and 0.05 with reference to bright (snow/ice) and dark (open water) surface types (Perovich, 1996). The resulting surface brightness of the typical surface types was similar to the observational datasets from autonomous radiation stations (Tao et al., 2024).

We co-located and compared the brightness data with in-situ surface albedo observations (Smith et al., 2021a; 2021b; Light et al., 2022). The co-location was realized by manually tracing the footprint of the albedo measurement lines, designated ROV4, RBB, and Bounty on the aerial orthomosaics (pink lines in **Figure 1**), and estimating the surface brightness at the closest pixel (0.5 m). The in-situ measured surface albedo was obtained via an Analytical Spectral Devices (ASD) spectro-radiometer, mounted on a 1.5 m handheld carbon fiber boom (Light et al., 2022). From the spectral albedo measurement, which ranged between the wavelengths of 350 nm and

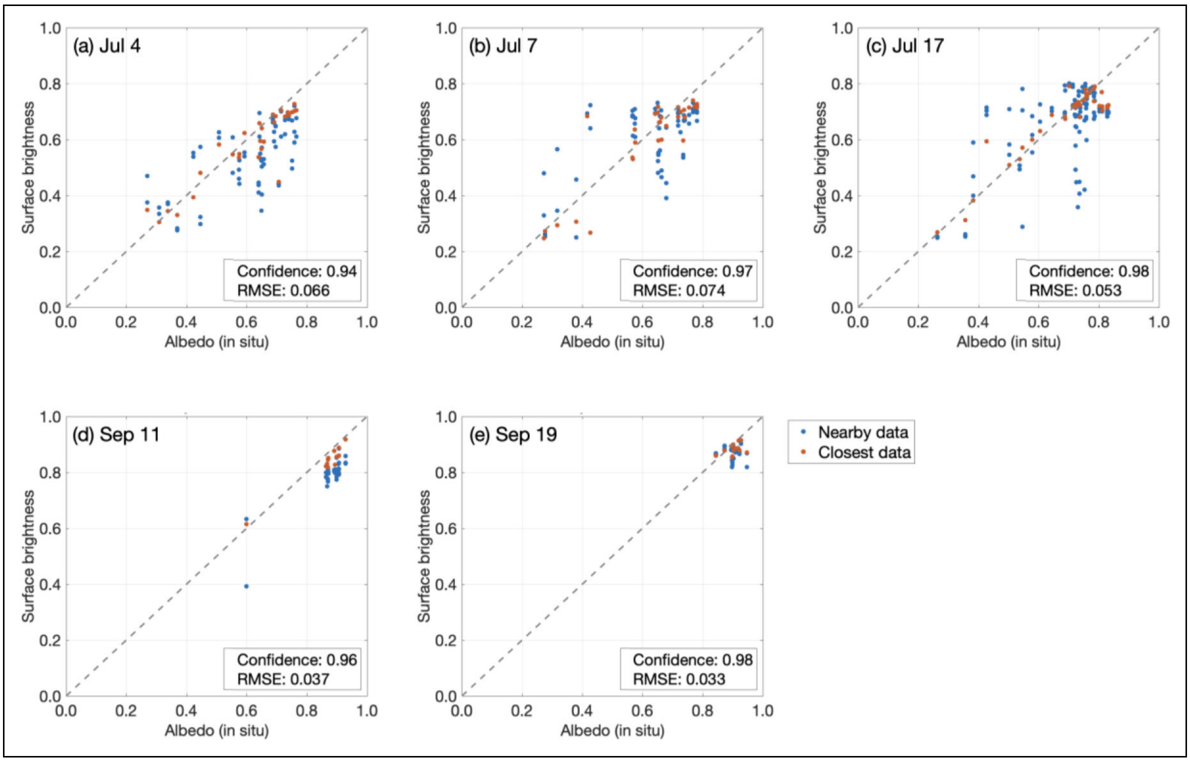

Figure 2. Correlation of calculated surface brightness and measured in-situ albedo. The blue dots are point measurements at the albedo lines (a) ROV4, (b) ROV4, (c) RBB, (d) Bounty, and (e) Bounty (locations shown in **Figure 1**; Smith et al., 2021a; 2021b). The in-situ albedo data shown here were integrated over the visible wavelength spectrum (400–700 nm). Red dots show data from the pixels surrounding the measurement points. The level of confidence and the root mean square error (RMSE) are shown and calculated from the closest data points (red dots).

2500 nm, we derived the surface albedo within the visible range (400–700 nm).

The comparison of in-situ albedo to the calculated surface brightness is illustrated in **Figure 2**. The in-situ albedo was integrated from the visible wavelength range. The best documented pairs of data are shown; while other lines of in-situ albedo were measured on the same days, they were not within the field of the aerial scans. For each in-situ measurement, the calculated brightness is shown for the closest (red) and the 4 next neighbor pixels (blue). We calculated the level of confidence and the root mean squared error values for the closest pixel only. The level of confidence was calculated as a ratio of the spatially closest pixel of the aerial image to the in-situ albedo observations, ranging from 0 to 1 (highest level). The level of confidence was about 95% for the visible wavelength range on all days, highlighting the robustness of the analysis approach in this work.

To calculate the MPF, a binary classification algorithm was applied to the grayscale aerial images of the sea ice surface. As illumination conditions varied daily, the threshold used to differentiate melt ponds from brighter ice surfaces was adjusted accordingly for each set of images. The grayscale image was generated from the RGB channels to isolate brightness, which is primarily driven by the reflectance, and a threshold value was determined based on the illumination and surface reflectance for that day. Pixels with grayscale values below the threshold were classified as melt ponds, while those above were classified as non-pond surfaces. This binary mask was used to calculate the MPF by determining the ratio of pond pixels to the total image pixels, allowing for proper accounting of the day-to-day variation in lighting conditions in the analysis. The location and margin of melt ponds are shown in the left panels of **Figure 3**.

In the first part of this study, we investigated the evolution in surface brightness of different sea ice surface types. This evolution is described along exemplary areas of 200 m × 200 m, which were chosen to represent differences in the distribution of bare ice and melt ponds and differences in their development over time. During melt season (**Figure 1a**), we selected three areas located near a large melt pond, referred to as "Mystery Lake" in other studies (e.g., Calmer et al., 2023). M-1 captured this large melt pond, while M-2 and M-3 were located near the multi-year ice and first-year ice coring sites. During freeze-up season, we selected two areas: F-4 was level ice with brighter melt ponds, and F-5 was deformed ice with darker melt ponds.

2.4. Solar radiative energy deposition into the sea ice surface

Another focus of this study was to examine the impact of the changes in the surface brightness on the radiative energy deposition. The energy deposition (within the visible wavelength range) was calculated at each pixel (0.5 m × 0.5 m). The energy deposition, expressed as an irradiance in W m^{-2}, was calculated from the mean of the

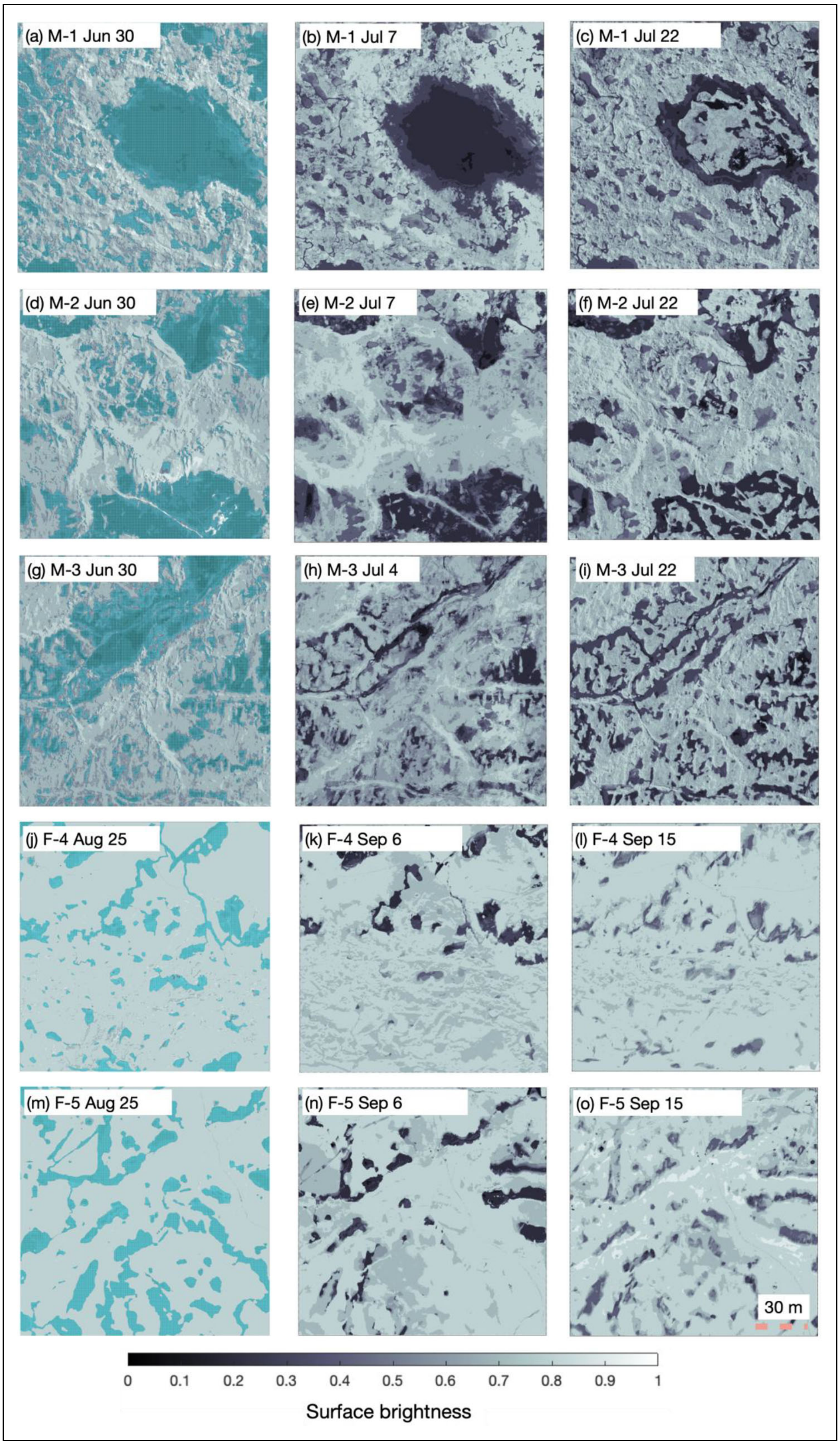

Figure 3. Seasonal evolution of surface brightness. (a)–(i) Areas M-1, M-2, and M-3 show melt and (j)–(o) F-4 and F-5 show freeze-up conditions in 2020. The light blue color on the panels in the left column illustrates the location and margin of melt ponds; changes in the melt pond fraction over time were used in the analysis. Major parts of the melt ponds drained between July 4 and July 22. During the freeze-up, observations were made on a different ice floe in the Central Arctic. In panels (j) and (m), August 25 was before the freeze onset (on August 26; Light et al., 2022). September 15 represents the day when F-4 and F-5 showed similar mean surface brightness. All images are 200 m × 200 m.

incident irradiance of the corresponding day (measured by the autonomous radiation station sited on bare ice, 2020R14 (Tao et al., 2024) multiplied by (1 − surface brightness)).

2.5. Spatial variability and representativeness

Variograms are a powerful tool in determining the scales of spatial variability by quantifying the spatial dependence between pairs of sampled points (Gómez-Hernández et al., 1999; Katlein et al., 2015; Meiners et al., 2017). The concept of variograms is to measure the level of similarity between pairs of points as a function of distance, with the hypothesis that, at a closer distance, the pairs of data are more likely to be related and to share similar surface conditions. The distance between the sampling data pair is known as "lag distance." The level of variability between the pair of data is described as the "semi-variance," calculated from the average squared difference between the data pairs. Typically, the semi-variance increases with larger lag-distance. For instance, a pair of data 5 m apart is more likely to have a higher spatial relation in terms of sea ice surface condition (e.g., in the same melt ponds) than a pair 50 m apart, where the surface condition is more likely to be random and possibly different. The role and size of sea ice surface features, such as melt ponds, can heavily influence the range of spatial correlation, as areas with larger ponds show longer ranges. Hence, whether the 5 m lags show stronger correlation than 50 m lags depends on the dominant spatial scale of features in the aerial images.

We used the MATLAB Central File Exchange function variogram (Schwanghart, 2023) and calculated the experimental semi-variogram with 100 bins of lag distance, each containing 2000 subsamples. The angle between the pairs was set to be random. We calculated the range, which described the lag distance reaching a value beyond which the variance did not increase and thus the data pairs were no longer related. Furthermore, we fitted a theoretical variogram to the calculated variance via a spherical function.

Variograms are a strong statistical tool in quantifying the spatial variability of the sea ice surface; however, the large number of sampling pairs limits its practicality in field observations. Therefore, we calculated the mean surface brightness over increments of area length, ranging from 25 m to 500 m on the ice floes. An increasing grid size includes a more variable range of surface conditions. When the area reaches a certain size, the distribution of the mean surface brightness converges to the mean surface brightness of the entire ice floe. As the observed ice area contained typical surface features like circular ponds, braided pond patterns, ridges, and so on, this approach helped to model and predict the spatial variability of surface brightness and representativeness of sea ice surface conditions, and will aid in future planning of drone observations of Arctic sea ice.

3. Results

3.1. General meteorological and sea ice conditions

Time series of air temperature, incident solar irradiance, and surface albedo and brightness are shown in **Figure 4**. Surface melt onset at the Central Observatory of the MOSAiC drift was on May 26, as described by Light et al. (2022) and Tao et al. (2024). After melt onset, air temperature fluctuated around the freezing point and remained positive after 20 June. On June 30, clear skies and lower air temperatures led to surface refreezing, resulting in a decrease in areal fraction of melt ponds. Also, small ponds appeared shallower, indicating ongoing lateral drainage or percolation despite freezing conditions (Webster et al., 2022). The initial freeze onset was on August 26 (Light et al., 2022) and air temperature turned to freezing again, reaching temperatures below −10°C. Solar incident irradiance reached its peaks in the second half of June, with a maximum value of 473.5 W m^{-2} on June 19.

In September, solar irradiance was lower than 100 W m^{-2} with several fluctuations. Note that the fall maxima were of the same magnitude as the summer minima. One reason for this similarity, besides the seasonality, is that the autumn drift was undertaken at much higher latitude than the summer drift (Nicolaus et al., 2022). Sea ice surface albedo dropped significantly after melt, while the variability increased drastically (see also Tao et al., 2024). The visible albedo values in our main study period (after 30 June) ranged from 0.55 to 0.80 for the melting period and between 0.70 and 0.90 for the freeze-up period.

During the previous freezing season, the average sea ice thickness grew 1.67 m (first-year ice) and 1.23 m (second-year ice) until mid-May (Raphael et al., 2024). The snow thickness reached the maximum in early May, surface melt began on May 26 (Lei et al., 2022; Tao et al., 2024). Following days of above-freezing temperature and precipitation, snow melted completely by June 25, and the ponded surface spread widely with a MPF of 10% (Lei et al., 2022; Webster et al., 2022; Tao et al., 2024). The sea ice floe underwent the advanced melting phase with some melt ponding events (e.g., **Figure 1a**). The mean sea ice thickness was 2.5 m in June (von Albedyll et al., 2022). On June 30, the MPF increased by 1% due to the clear sky condition and higher temperature; the maximum melt pond coverage was 21% on July 26 (Webster et al., 2022).

In late summer in the central Arctic, the sea ice and surface conditions were more complex due to the various weather conditions and events. The mean sea ice thickness was 1.02 m. The first snow event was on August 25, followed by above-freezing temperatures and more snow events, until September 1 when the sea ice was continuously under freezing condition (Rex and Metfies, 2023). Then, the sea ice surface showed more pond freezing, snow, and rain on snow (Light et al., 2022).

3.2. Evolution of sea ice surface brightness during melt season

Here, we first evaluate the seasonal evolution of sea ice surface brightness over the selected areas (M-1, M-2, and M-3; **Figure 1**) in the late melt season. **Figure 3** shows the surface brightness, as calculated for the selected regions and different dates based on Section 2.3. Along the left column of panels in **Figure 3**, we highlighted the location of surface melt ponds via the light blue mask to show the MPF on the sea ice surface before the drainage event

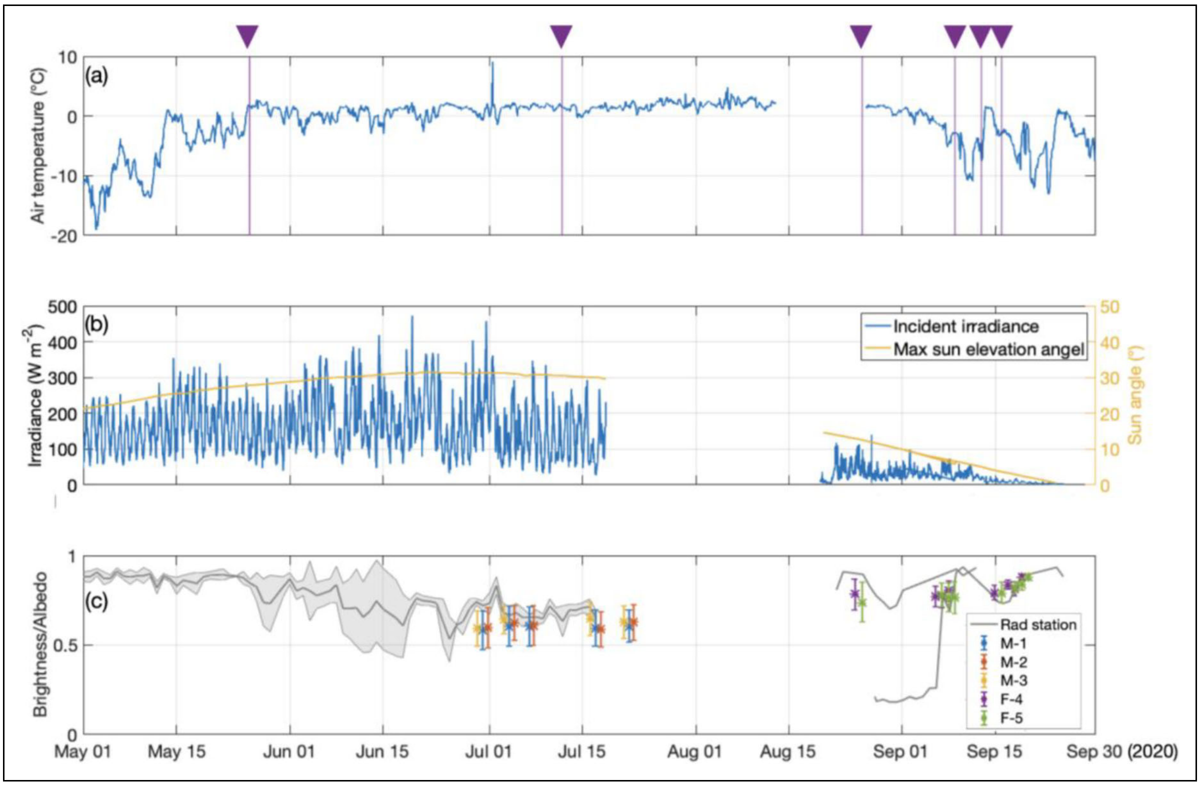

Figure 4. Meteorological and surface conditions during the observational period in 2020. (a) Air temperature from Snow Buoys 2019S86 (until August 13) and 2020S106 (after August 24). Purple triangles above the panel mark the dates of melt onset (May 26), melt pond drainage (July 13), initial freeze onset (August 26), snowfalls (September 9 and 13), and continuous freeze onset (September 16; Light et al., 2022; Webster et al., 2022). (b) Incident (hourly) solar irradiance from radiation stations 2020R11 (May 1 to July 18), 2020R21 (September 12–30), and 2020R22 (August 21 to September 12), as well as solar elevation angle. (c) Measured surface albedo and calculated brightness. Mean (gray line) and standard deviation (gray area) of surface albedo were calculated from spectral radiation stations 2020R11, 2020R12, and 2020R14 during melt season and stations 2020R21 and 2020R22 during freeze-up. For the surface brightness, the mean and standard deviation are calculated for areas (each 200 m × 200 m) M-1, M-2, and M-3 (melt season) and F-4 and F-5 (freeze-up). Note that these data are plotted with a delayed/advanced time-stamp (0.75 days) to show the comparison more clearly, while in reality, each set for a given area is from the same survey.

(**Figure 3a**, **d**, and **g**). The seasonal evolution of the surface brightness is illustrated based on distribution probability in **Figure 5**.

On June 30, areas M-1, M-2, and M-3 showed different sea ice and surface conditions, with surface MPFs of 40%, 36%, and 30%, respectively. The surface brightness ranged between 0.22 and 0.80. In early July (July 4 and 7), the MPF decreased at M-1 by 5% (from 39% to 34%) and at M-3 by 4% (from 30% to 26%), while the MPF remained constant at 35% at M-2. After mid-July, the MPF decreased strongly at all three sites: on July 17, M-1 and M-2 both showed a decrease of 12%, and M-3 of 8%. At the end of July, the MPF became similar for all three sites, with surface brightness ranging between 0.61 (M-1) and 0.63 (M-2 and M-3).

3.3. Evolution of surface brightness during freeze-up season

The seasonal evolution of surface brightness during the freeze-up season is illustrated by imagery in **Figure 3j–o**, and distribution probabilities in **Figure 6**. From late August to mid-September, in only 2 weeks, the sea ice surface brightness increased rapidly with the refreezing of the sea ice surface and the accumulation of an early snow.

In late August, the ice floe was a mix of bare, level first-year ice, melt ponds, and deformed ice (see also Lei et al., 2022; Webster et al., 2022). F-4 was dominated by level sea ice with bright melt ponds (MPF of 15%), and F-5 was a more deformed sea ice surface with darker melt ponds (23%). A large portion of the F-4 and F-5 areas were bright bare ice and snow, and the mean surface brightness was 0.78 and 0.74. After freeze onset at the sea ice surface (August 26), both F-4 and F-5 showed a mean surface brightness of 0.77. The MPF decreased below 5% in both areas. There were some changes in the mean surface brightness due to precipitation, which also increased its spatial variability temporally. After mid-September (**Figure 6**), the sea ice surface showed a higher brightness (mean of 0.79) with minimum MPF. Summarizing the evolution of surface brightness during the summer–autumn transition (freeze-up), we find that this transition was characterized by more rapid changes with a reduced spatial variability compared to the spring–summer transition.

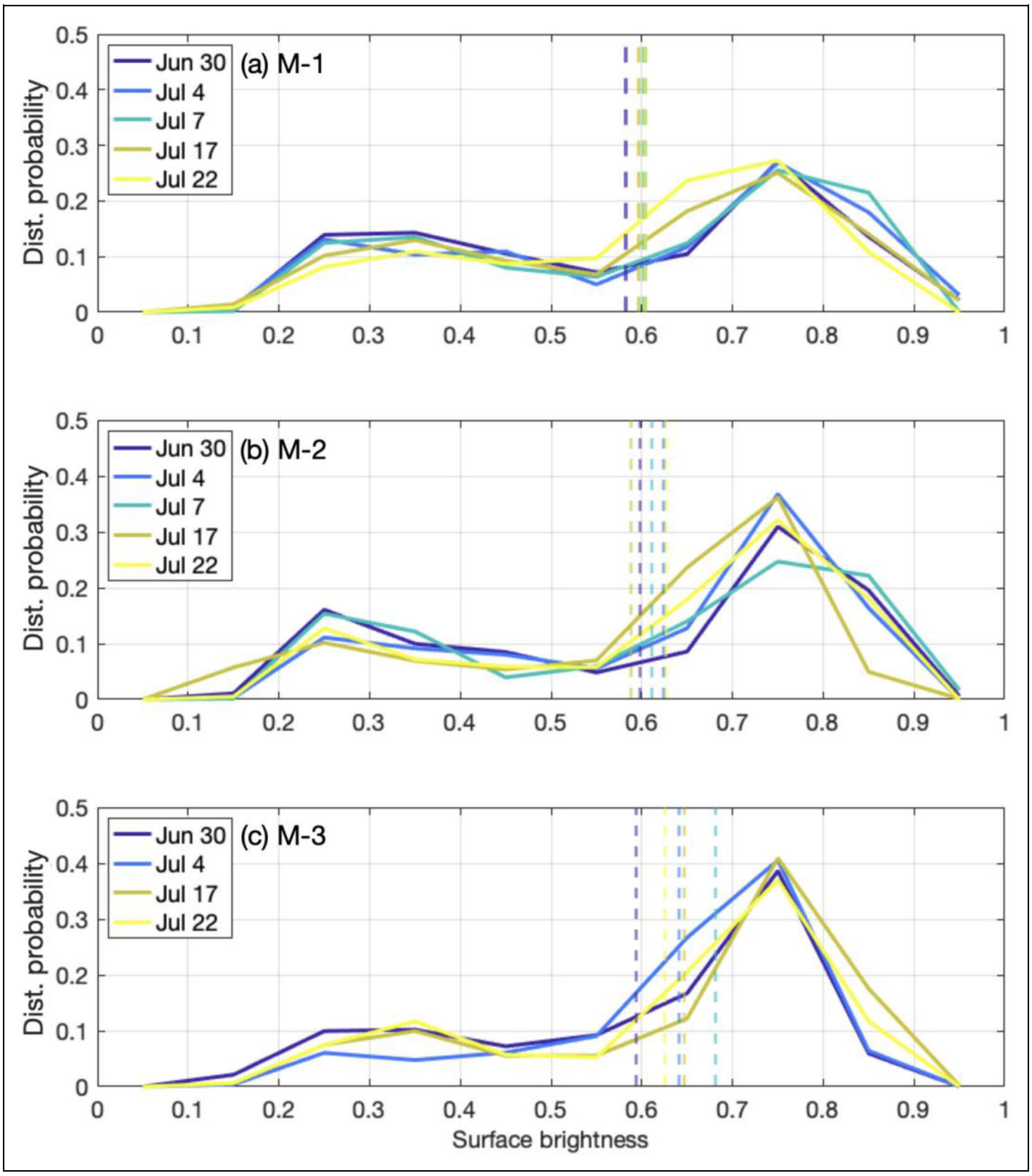

Figure 5. Surface brightness distribution probability (histograms) during the melt season. (a) Area M-1, (b) area M-2, and (c) area M-3. The dashed vertical lines show mean surface brightness on the given day. See **Figure 1a** for the location of each area. Note that in panel (c), July 7 is excluded from the M-3 time series due to incomplete imagery.

3.4. Seasonal evolution of solar radiation fluxes into the surface

The fluxes of solar short-wave radiation into sea ice are a main component of energy deposition into the ice during summer. The amount of visible radiative energy deposited into the sea ice surface was calculated from the mean of the incident irradiance $E_i(t)$ (measured by the autonomous radiation station, 2020R14; Tao et al., 2024) of the corresponding day (*t*) onto the surface (sea ice and/or snow); the surface brightness was calculated from RGB photographs over the visible spectrum, 400–700 nm:

$$E_{\text{ice}}(t) = E_i(t) \times [1 - \text{surface brightness}(t)]$$

Accordingly, we calculated the total energy deposition $Q_{\text{ice}}(t)$ into the area (*a*) of sea ice and snow surface:

$$Q_{\text{ice}}(t) = E_{\text{ice}}(t) \times a$$

Figure 7 shows the means of visible radiative fluxes reflected at the surface and deposited into the sea ice, as well as the mean surface brightness for areas M-1, M-2, and M-3 during the melt season (**Figure 7a**), and areas F-4 and F-5 during the freeze-up season (**Figure 7b**).

During melt season, the day-to-day variability of energy deposition was high, ranging from 41.7 W m^{-2} to 95.8 W m^{-2} within the 3 weeks of observations. On the same day, the total energy deposition varied little (<10%) across the three areas. For example, both M-1 and M-2 showed a similar energy deposition of 42 W m^{-2} and 42.75 W m^{-2} on July 17, which was 20% higher than at M-3. The energy deposition was more than double of that just 5 days later on July 22, with a difference of 5% between the areas. The effects of changes in the surface properties were small compared to the effects of

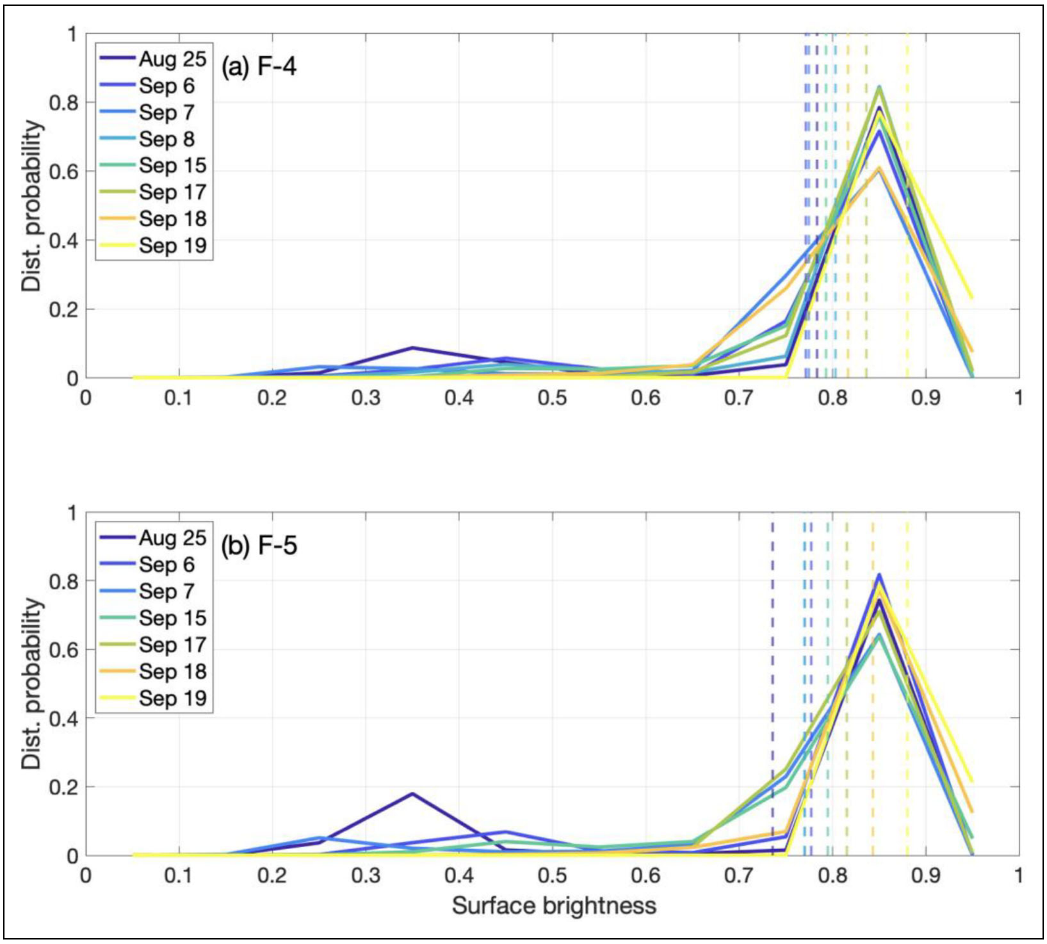

Figure 6. Surface brightness distribution probabilities (histograms) during the freeze-up season. (a) Area F-4 and (b) area F-5. The dashed vertical lines show mean surface brightness on the given day. See **Figure 1b** for the location of each area.

temporal variability irradiance, which also shows that the size of the areas selected was sufficient.

During the freeze-up season (**Figure 7b**), energy deposition decreased significantly as surface brightness increased. On August 25 (**Figure 7b**), F-4 and F-5 showed mean energy deposition of 19.6 W m^{-2} and 23.7 W m^{-2}, respectively. Within days, the energy deposition of both M-4 and M-5 decreased by 65%. On September 6, the energy deposition decreased further to the similar values of 6.7 W m^{-2} and 6.5 W m^{-2}, respectively, as the sea ice surface had refrozen quickly, within days after the freeze onset. The mean surface brightness rose rapidly to over 0.80 after mid-September, indicating the transition to a more reflective, snow-covered surface. By mid-September, the surface brightness in both areas converged, as the ice floes refroze and spatial differences between melt ponds and bare ice diminished.

3.5. Spatial variability of fluxes on small scales

So far, we have described the surface brightness and resulting short-wave radiation fluxes into the sea ice surface as integrals over the individual areas, each 200 m × 200 m in size. **Figure 8** shows, at a smaller scale, the daily mean of energy deposition into the sea ice over the observational periods of the melt season in areas M-1 to M-3 and freeze-up seasons in areas F1 and F2. These depictions highlight the spatial variability within each area, and thus the variability on smaller scales than the 200 m × 200 m areas.

During the melt season, the sum of surface solar radiative energy deposition was within 6% at all three locations (**Figure 7**) despite the vastly different surface conditions. However, within each area, the spatial heterogeneity of the surface caused large differences. The energy deposition at M-1 ranged from a daily average of 5.5 W m^{-2} on bare ice to 94 W m^{-2} at the large melt pond "Mystery Lake" (**Figure 8g**). The range of energy deposition at M-2 and M-3 was also wide, but not as wide as at M-1. Their minima were 126% and 170% larger, respectively, than at M-1, and their maxima were 90% and 93%, respectively, of that from M-1 (**Figure 8a–c** and **g**). Melt ponds at M-1 had a stronger and longer-lasting impact on the energy deposition than at the other two locations.

During the freeze-up season, the mean of energy deposition was less than 33% of melt season, due to the low incident irradiance and high surface brightness. Due to darker melt ponds, F-5 had a 7% higher energy deposition than the F-4 site (**Figure 7**), and most energy was accumulated in late August. Within both sites, the spatial distribution of energy deposition remained associated with the location

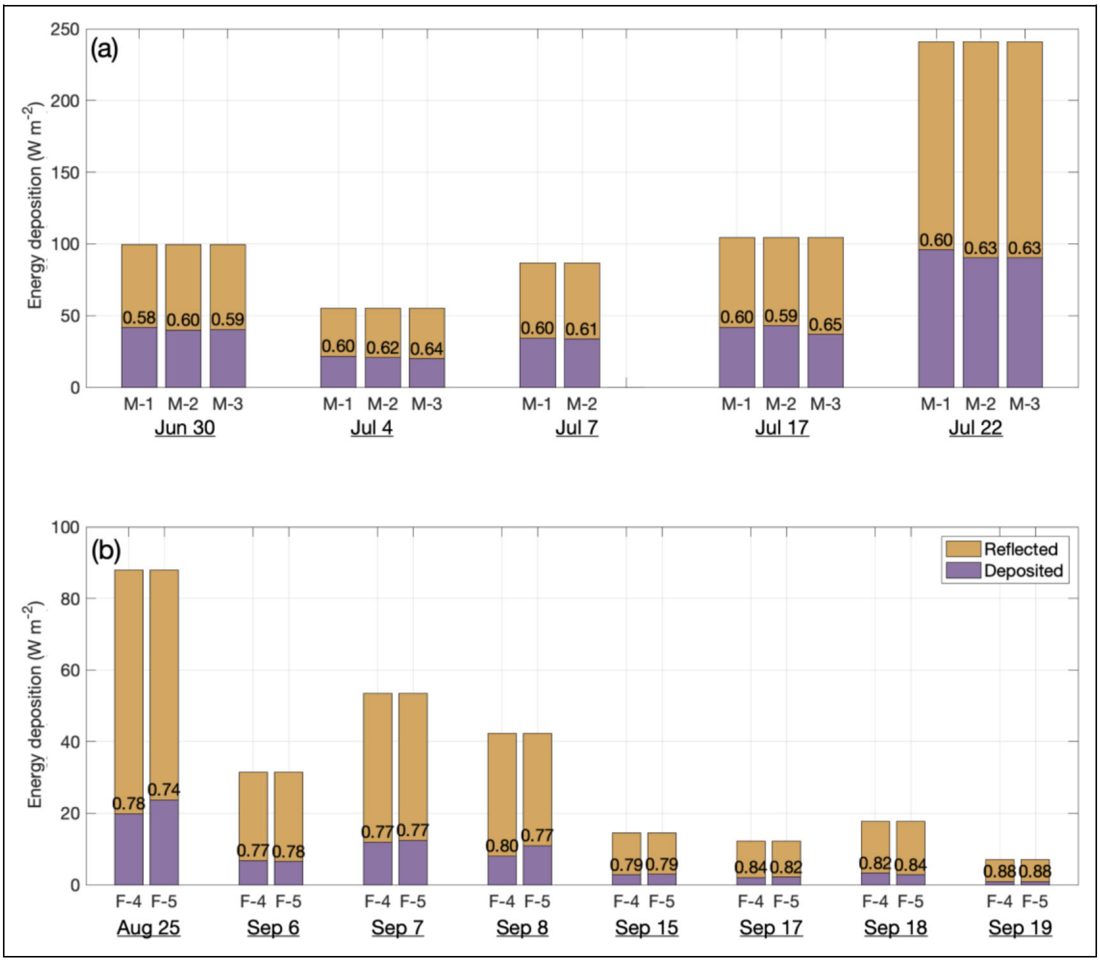

Figure 7. Seasonal evolution of radiative fluxes and surface brightness at visible wavelength spectrum. (a) Melt season and (b) freeze-up season. The reflected and deposited radiative energy was calculated as the sum of each area (**Figures 1** and **3**). The mean surface brightness of each image is given as a number in each bar. In panel (a), July 7 of M-3 was excluded due to incomplete imagery. Note the different scales of the y-axes in panels (a) and (b).

of (former) melt ponds (**Figure 8d** and **e**). Large parts of the areas accumulated less than 10 W m^{-2} day^{-1}.

3.6. Role of melt ponds in radiative fluxes

During the transitional seasons, the strong changes in MPF were the primary driver of changes in surface brightness and the partitioning of solar radiative energy. **Figure 9** compares radiative fluxes into the sea ice surface through ponds and white ice, as well as the mean surface brightness and MPF for selected dates.

The dates reflect different stages of the melting and refreezing, emphasizing how surface conditions control the solar energy fluxes into or through the ice. On June 30, MPF was 37% and the mean surface brightness was 0.58 (**Figure 9a**). Despite covering just over one-third of the surface, melt ponds accounted for 61% of the total solar energy flux into the sea ice, highlighting their strong influence on energy deposition during the melt season. As the Arctic experiences highest solar irradiance during this period, small changes in MPF have large impacts on the total energy flux into the sea ice and the accumulation of heat for sea ice melt. On July 22, the mean MPF decreased to 28%, because parts of the surface had already drained again and the mean surface brightness increased to 0.64 (**Figure 9b**). Despite the reduction in melt pond coverage, these ponds still accounted for 50% of the total solar energy influx into the ice surface, which shows how the dark pond surfaces continued to drive a substantial portion of solar energy deposition and contributes to continued significant melting.

As the Arctic transitioned from summer to autumn, as shown in the comparison between August 25 and September 19 (**Figure 9c** and **d**), the sea ice surface shifted from a melting regime to refreezing. By August 25, MPF decreased to 19% due to further refreezing and the onset of surface freezing, while the dark pond surfaces continued to absorb 51% of the total solar energy influx, more than half of the energy in this stage at the transition to freeze-up. The mean surface brightness increased to 0.75, mostly as a consequence of the brighter surface of the un-ponded ice. By September 15, most melt ponds had refrozen and the MPF had dropped below 5%. The mean surface brightness reached 0.79, and the radiative energy deposition decreased by more than 10-fold, signaling rapid transition to the autumn and winter season.

These results show how the change in melt pond cover and status controls the radiative energy deposition into

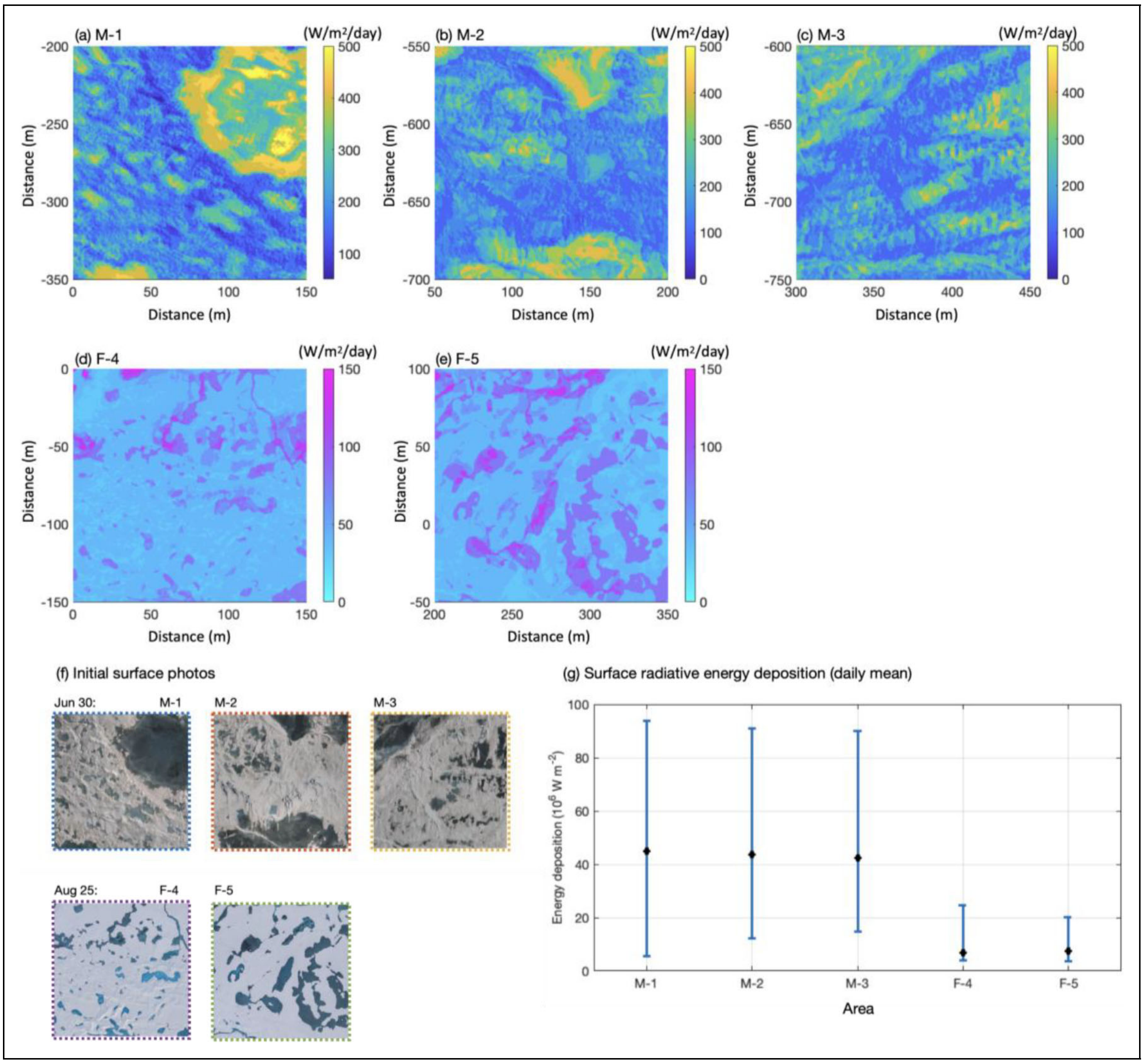

Figure 8. Surface energy deposition during melt and freeze-up seasons. Daily mean fluxes for (a)–(c) the melt season in areas M-1, M-2, and M-3, with "Mystery Lake" visible in (a), and (d),(e) the freeze-up season in areas F-4 and F-5. The radiative energy deposition was computed from surface brightness at visible wavelengths. Note the different color scales for the two seasons, representing vastly different solar irradiances. (f) Surface photos in true color for the areas in panels (a)–(e), as enlarged from **Figure 1**. (g) Mean (black dots) and range of surface energy deposition (blue bars) during the melt and freeze-up seasons.

the sea ice surface. During the melt season, the combination of peak incident irradiance and high MPF dominated the radiative energy budget. When transitioning to autumn, the decreasing incident irradiance and smaller MPF during autumn lead to reduced energy deposition, causing the sea ice to refreeze.

4. Discussion

4.1. Impacts of different surface types on deposition of solar radiation

The spatial variability of solar radiative energy deposition across different surface conditions plays a crucial role in understanding how energy is distributed on sea ice throughout the melt and freeze-up seasons. During summer, the evolution of melt ponds impacts both the spatial variability in surface fluxes and the total amount of absorbed energy.

Ultimately, the distribution of melt ponds resulted in a similar energy deposition amongst the three areas examined. For instance, the entire M-1 area showed 4–6% higher energy deposition than M-2 and M-3. While the areas also showed a different pattern of energy deposition, M-1 showed a strong contrast between lower and higher deposition. The latter was scattered mainly around the center and the outskirts of the "Mystery Lake." M-2 also showed a contrast in surface deposition associated with the melt pond locations. At M-3, rather than having strong deposition features, such as the large melt pond "Mystery Lake" of M-1, the surface deposition had a weaker contrast than the other two locations but a similar sum of absorbed energy.

During the freeze-up season, the reduced incoming solar irradiance limited the energy deposition at the sea ice surface. Together with the higher but less variable surface brightness, it also reduced the spatial variability of energy deposition into the sea ice. Overall, less than

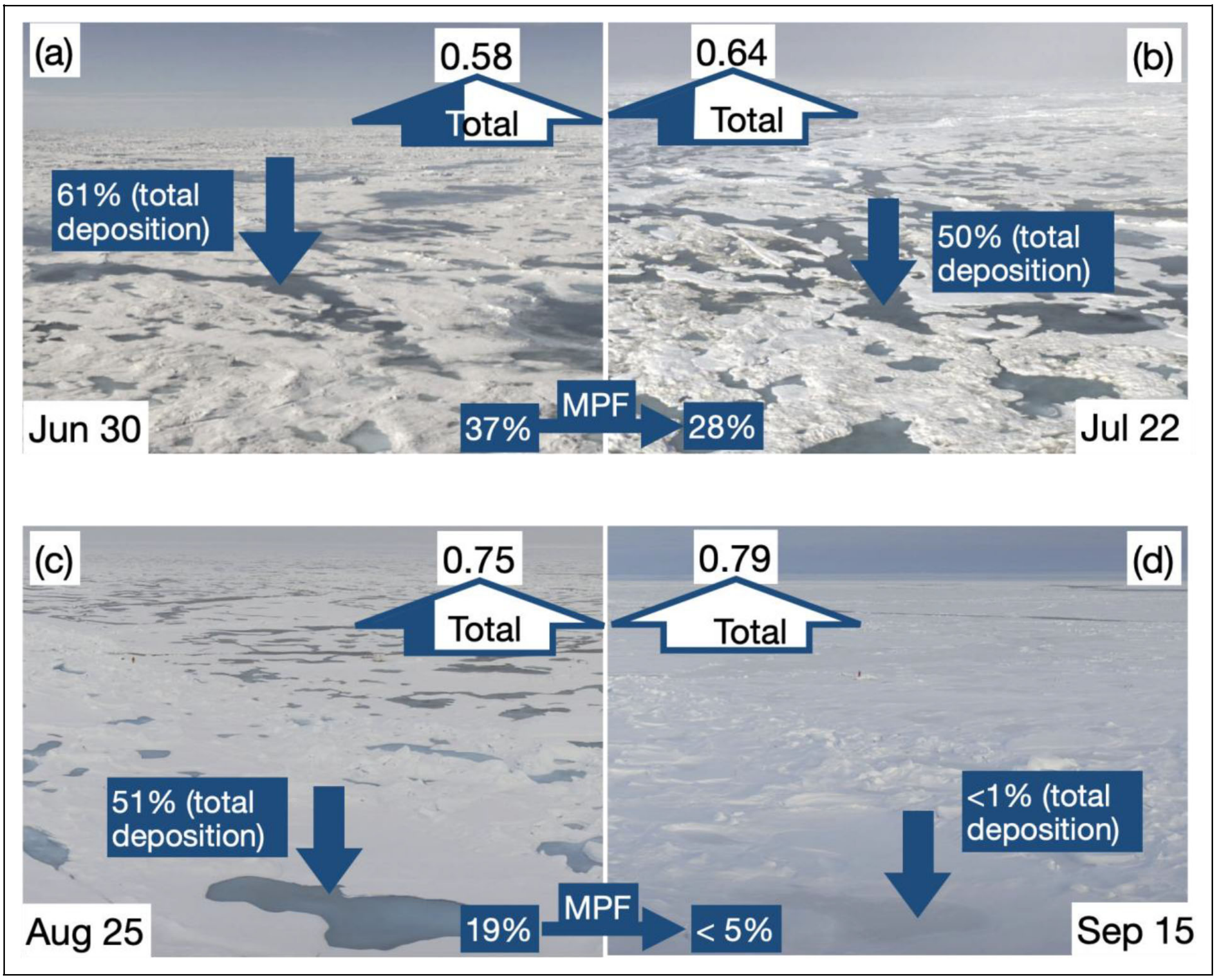

Figure 9. Changes in energy deposition and distribution over sea ice. Seasonal evolution from (a) June 30 to (b) July 22, (c) August 25, and (d) September 15. The wide upward arrows show the total mean surface brightness within visible wavelengths, and the portion of blue shade in these arrows represents the melt pond fraction (MPF), which is labeled. The downward arrows show the mean percentage of radiative energy deposition via melt ponds to the entire areas of 200 m × 200 m.

33% of the July energy was deposited in August and September, also leading to a sharp decrease in the total energy absorbed by the sea ice during the freeze-up period.

This study used 200 m × 200 m large areas in order to minimize the impact of small-scale variability. Hence, the difference between areas is rather small and a high variability is covered within each area. At the same time, the influence of spatial variability is expected to be a function of the size of the sampling area. This size function becomes obvious when sub-dividing the areas into smaller grids. For instance, sub-dividing M-1 into a 10 m × 10 m grid, the mean energy deposition over the study period would range for the individual grid cells between 14 W m^{-2} day^{-1} and 88 W m^{-2} day^{-1}, resulting in a difference of over 600%. Even within a 100 m × 100 m grid, the difference in the mean energy deposition (per 10 m × 10 m grid cell) would still vary by more than 300%, where the mean ranges from 22 W m^{-2} day^{-1} to 70 W m^{-2} day^{-1}. These aspects of scales are further analyzed and discussed in Section 4.3.

The observed spatial variability in surface brightness within the different areas is a result of various ice surface processes. In June and July, melt pond formation and evolution, including drainage, were the key elements. In parallel, the white ice underwent some changes, which may be expected to have minor impacts compared to the pond histories. The drained scattering layer is known to be rather constant in albedo and also in brightness (Smith et al., 2022; Macfarlane et al., 2023). One important aspect not included in our areas is the transition to open water and reduction in sea ice concentration. This aspect obviously has a huge impact when studying surface brightness and albedo, even on larger scales. In August and September, two processes controlled the brightness evolution. The re-freezing of the surface had stronger effects (in terms of brightness) on the ponds than on the white ice. The increase in pond surface brightness was 0.32 and that of white ice, only 0.17. In addition, the re-freezing of the ponds is the necessary condition for snow accumulation on the ponds. Snow- and rainfall caused strong day-to-day changes. Sea ice dynamics (ridging, lead formation) also have strong impacts on surface brightness but are not included here, as we chose stable areas of the floe. Otherwise, they would impact the brightness directly and indirectly, the latter because of differences in snow accumulation compared to level sea ice.

Understanding the impact of all these processes on different scales is crucial to determining the energy budget of the Arctic. However, the calculated surface brightness of bare and snow-covered ice is more accurate and easier to evaluate than over melt ponds. Also, the smaller bias observed in September is only valid for bright surface due to the lack of other surface conditions, such as melt ponds. In future, including more in-situ observations as a validation would help improve the precision of this approach. Tracking known targets (e.g., open water, white ice) could also improve the precision of calculated surface brightness.

4.2. Comparison with albedo studies on different scales

In this study, we calculated the surface brightness as a function of time and area length and investigated its impact on the energy absorptivity. However, the calculated surface brightness is not strictly albedo. An uncertainty of surface brightness smaller than 10% is expected (e.g., **Figure 2**) and considered to be sufficient to investigate the scales of surface spatial variability and its effect on the sea ice surface energy budget.

Many previous studies of surface albedo focused on single-point and line measurements (e.g., Perovich, 2005; Nicolaus et al., 2010; Perovich and Polashenski, 2012). During the MOSAiC expedition, Light et al. (2022) and Tao et al. (2024) conducted in-situ observations of the sea ice surface albedo. Understanding the representativeness of the observation and the scale of spatial variability is a crucial step to bridging the local observation to larger satellite and modeling scales. Tao et al. (2024) observed the seasonal evolution of sea ice albedo and under-ice transmittance from May to mid-July with three stations. They found a strong variability after the surface melt onset on May 26, which was introduced mostly by ponding events, which were very different at the three sites. Noticeably, after late June, all three stations showed a weathered surface layer with mean surface albedo returning to a mean of 0.68 from the minimum of 0.56. However, this case did not apply to the entire ice floe. For instance, Light et al. (2022) investigated the albedo of individual ice types along survey lines with multiple points of measurement. Albedo at visible wavelengths increased in late June and early July due to melt pond drainage and a subsequent overall decrease in the fraction of ponded ice (see also Webster et al., 2022). Toward August, albedo decreased again with increasing pond depth and extent. Overall, along the survey line, the spatial variability increased with the progression of the melt season.

In this study, we also observed a surface drainage after July 7 (**Figure 3**). Making use of the areal approach, we identified strong changes in parts of the area (where the pond drained), while the mean surface brightness of the entire area decreased only by less than 10%. Larger sampling areas include a wider range of sea ice surface types, thus resulting in a value closer to the large-scale changes.

Calmer et al. (2023) investigated the summer sea ice surface conditions (e.g., MPF, albedo) with drone measurements, using surface imagery and stabilized pyranometers. Based on their albedo distribution functions, a shift occurred from 0.60 in early July to 0.30 at the end of July, with the MPF increasing by 8%. These results differ significantly from ours, where surface brightness, the proxy for albedo, had no trend and variability was small between the areas but large within each area. The reason for this difference is mostly the observational approach. Their flights were performed centered over melt ponds. With increasing flight altitude, the sampling area became larger; subsequently, the albedo value converged with the entire image. However, the central melt pond remained a dominant feature and only albedos at high flight levels covered footprints of 300–600 m. This comparison shows the important role of the choice of the sampling location and the observed area when aiming for and comparing larger-scale estimates of surface albedo (brightness). At the same time, the use of aerial imagery yields even larger survey areas and can produce more representative results for larger regions and support further up-scaling (e.g., Fuchs, 2023).

4.3. Relating different scales of spatial variability

The presented approach of large areas 200 m × 200 m in this study showed a higher spatial variability than may be derived from several point measurements, such as radiation stations at fixed points. For instance, **Figure 4c** compares the mean surface brightness to the albedo measurements from three radiation stations in Tao et al. (2024). The stations observed a higher mean albedo than the areas of this study. Also, the variability across the three stations is at the upper limit of the brightness measurements in the presented areas. This result is due to the choice of the deployment sites of the stations on bare ice and avoiding melt ponds with lower albedo. In general, melt ponds are often under-represented in point measurements, which generally include fewer surface types and conditions. However, the advantage of stationary measurements is the much higher measurement frequency.

Our results may also be compared to albedo transect lines of the same ice floe, as published in Light et al. (2022; **Figure 7**). The albedo lines show a similar evolution of the surface with day-to-day variability but no trend in July. At the same time, the measured mean albedo was lower (0.35–0.60) then the brightness in this study (0.5–0.7; **Figure 4c**), but with a similar range of variability of 0.2–0.3.

To further investigate the necessary scales of variability, **Figure 10** shows variograms of the surface brightness, taken over an area of 600 m × 600 m centered on the ice floe. The variance increases with the lag distance between a pair of data (with random direction and position), until the lag distance reaches a threshold ("range" in **Figure 10**), where the pair is unrelated to each other; that

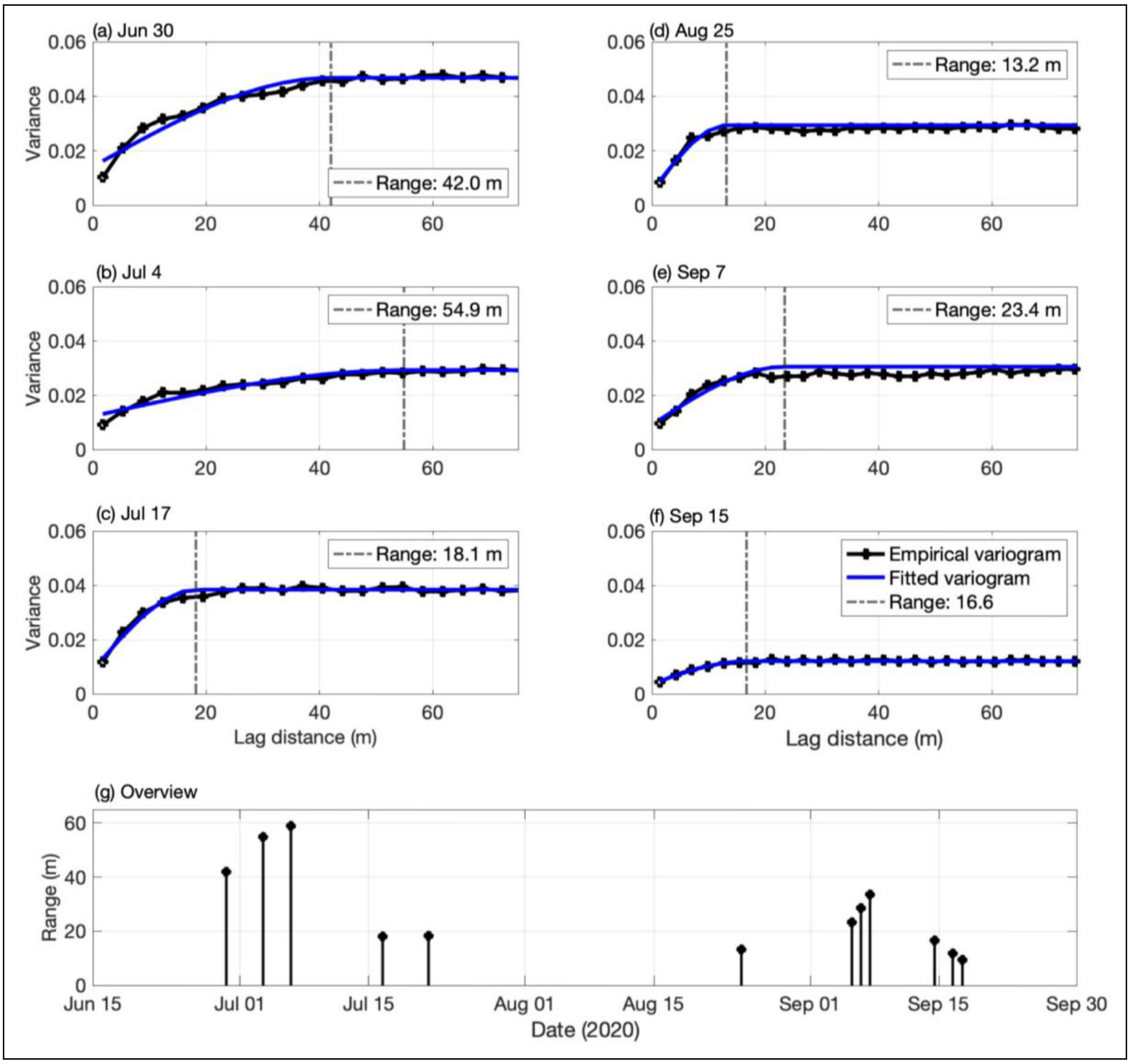

Figure 10. Variance of surface brightness during melting and freeze-up seasons. (a)–(c) Variograms computed for areas of 600 m × 600 m during the melting season and (d)–(f) areas of 500 m × 500 m during the freeze-up season. The different sizes of the sampling areas were due to the different sizes of the ice floes sampled; see **Figure 1**). Shown are the empirical variograms (black), range (dashed vertical lines), and fitted theoretical exponential histograms (blue lines). (g) Overview of the seasonal evolution of ranges from all surfaces.

is, the range correlates positively with the spatial variability.

During the melt season, the range of the variance increased from 42 m to 59 m on July 7, indicating that the spatial variability of the sea ice surface increased. After surface drainage on July 17, the range of the variogram decreased again to 18 m and remained almost constant until July 22. This pattern shows that the decreasing pond fraction reduced the length scale of the surface spatial variability in the latter half of the melt season. During freeze-up, the variability showed an increase from 27 m to 86 m from late August to early September, reaching the maximum of 84 m on September 7 due to the large open water fraction at the edge of the sampling area. The range of the variance decreased with the refreezing of the surface and the snow cover. The range of variance decreased rapidly with re-frozen surface and snow to about 20 m in September 15 (**Figure 10**). On September 18, the range was 11 m. The scale of variability during the early melting/freeze-up process was significantly higher than that from previous studies (e.g., range of 10.6 m in Katlein et al., 2015), as our study included more heterogeneous surface types (e.g., M-1).

Variograms can be used to aid in planning future observations, such as measurements along transect lines. However, they do not fully represent the spatial variability of an area, especially considering the large sample size and demand for computational power, which limit their usefulness in field applications. **Figure 11** shows the mean surface brightness of areas with lengths from 25 m to 250 m. The sampling area is a square with length of 600 m and 500 m for the melt and freeze-up seasons, centered on the ice floe (same as for the variograms in **Figure 10**). The difference in area length was due to the difference in size of the ice floe (**Figure 1**). For each group of area length, various means were calculated for the sampling area, and their distribution is shown with respect to

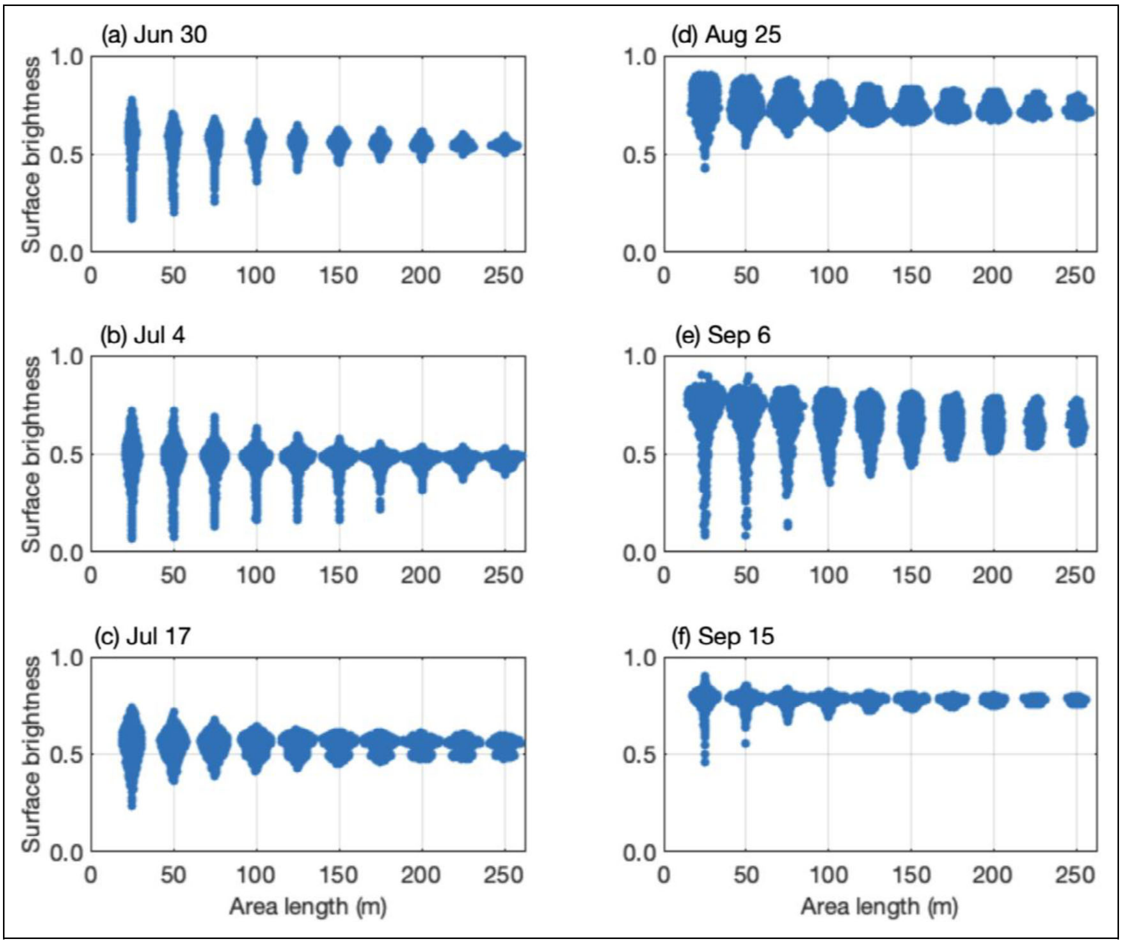

Figure 11. Areal averaged densities of surface brightness with increasing averaging sizes. The areas are squares, with area length indicating all sides. The vertical extent of each cluster represents the range of the mean surface brightness, and the width of each cluster represents the offset (distribution) of the means.

the width of each group. A wider distribution suggests higher surface spatial variability.

During the melt season, the mean surface brightness at a small 25 m grid can vary from 0.12 to 0.78 (**Figure 11**). As the size increased and a broader range of the sea ice and snow surface was included, the mean surface brightness showed a more clustered distribution. For instance, on June 30, the mean surface brightness of a 200 m grid ranged between 0.48 and 0.65. After the surface drainage event, the distribution of the mean surface distribution of the 25 m grid became more clustered. However, the difference between mean albedo over the 200 m grid was still larger than 0.15. During the freeze-up season, the distribution of the mean surface brightness became smaller. On August 25, over a small area of 25 m grid, the mean surface brightness ranged from 0.49 to 0.89. At a larger scale (e.g., 200 m area length), the range of the mean surface brightness was 0.72 to 0.85. On September 6, the mean surface brightness shows a large range at small scales. After mid-September, the scale of variability in the mean surface brightness reached a minimum.

This analysis confirms that the choice of 200 m × 200 m areas in this study is representative of the existing spatial variability on the entire floe during melt season, the time when spatial variability is highest. Results from areas of this size or larger on the ice floe will find the distribution of mean surface brightness values that is within 10% of the mean surface brightness of the ice floe, for example, on June 30, the maximum and minimum mean of the 200 m × 200 m area were 0.60 and 0.49, within ±10% of the mean of the ice floe (0.54). The mean incident irradiance was 99.6 W m^{-2}, which means that the minimum and maximum radiative energy deposition were 39.9 W m^{-2} and 50.8 W m^{-2}, with the range spanning roughly 11% to 13% around the mean energy deposition into the surface.

Measurement of surface brightness (and albedo) should cover similar scales to include the existing spatial variability. Perovich et al. (2002) determined that at SHEBA, the representative scale was roughly tens of kilometers over a larger scale across multiple ice floes. At the same time, studies outside the main melt season, when melt ponds are less or not developed may also use smaller areas and still cover the variability. Future work on the sea ice surface brightness and radiative energy budget should include spatial scales of at least 200 m × 200 m.

4.4. Uncertainties

Precise observations of surface albedo require direct measurements of incident and reflected irradiance. This requirement is very challenging, in particular for mapping larger areas and to repeat the mapping over the seasonal cycle. Understanding the seasonal changes and spatial variability in sea ice surface albedo is the key to understanding the shortwave radiative fluxes. In this work, we used the surface brightness, a proxy to albedo, to evaluate the impacts and scales of sea ice surface spatial variability in the radiative energy budget. The surface brightness used in this study showed a confidence level of 95%, when comparing to in-situ albedo (Smith et al., 2022). Also, Fuchs (2023) compared the three CANON color-band intensities (relative spectral response applied to ASD measurements) with co-located broadband pyranometer-derived albedo, and the margin of errors were below brightness differences.

Using RGB images to calculate surface brightness can cause uncertainty in calculating radiative energy deposition, as the spectrum focuses on the visible wavelength range. While surface brightness provides a robust proxy to investigate the changes and impacts of sea ice surface variability, it does not account for the lower reflectance of sea ice, snow, and melt ponds in the near-infrared domain. Visible-band brightness overestimates the radiative energy deposition into the sea ice surfaces by about 5% over a bare ice surface and over 20% over a melt-ponded surface (comparing to observations from radiation stations 2020R12 and 2020R14 in Tao et al., 2024), due to the strong absorption of near-infrared radiation by liquid water. In this study, the irradiance, brightness and albedo presented were consistently integrated over the visible range. We recommend future work to incorporate spectral correction factors or use hyperspectral and broadband data for more accurate surface energy assessments.

Another uncertainty is due to solar inclination, which changes the apparent brightness of melt ponds. As the solar angle becomes lower in August and September, light reflected from water surfaces (like melt ponds) appears brighter compared to mid-summer, even if the MPF and irradiance have decreased. This increase in the surface brightness due to the solar angle can influence the interpretation of RGB-derived brightness, leading to the overestimation of the energy deposition.

Additionally, RGB-based surface brightness detection may underestimate the presence of subsurface melt ponds, particularly when they are covered by a thin, refrozen ice lid and snow. These subnivean melt ponds can be optically similar to surrounding snow-covered ice, despite potentially storing a large volume of meltwater beneath. This similarity introduces uncertainty into the surface albedo representation and the estimated radiative energy budget, as such hidden ponds may still absorb solar radiation through the translucent ice and snow layers. Future work could integrate spectral or thermodynamic data to better detect and quantify these features.

In this study, we focused on the scales and impacts of sea ice floes without considering the impacts from leads, deformed ice and ridges, or ice floe sizes. Particularly during the sunlit season, the different sea ice conditions and sizes of the floes can influence the scales of sea ice surface variability. However, the approach we have introduced here can be adjusted to the sea ice conditions. Additionally, the influence of surface elevation variability, or freeboard variability, could also introduce uncertainties in the interpretation of surface brightness, especially with the presence of melt ponds and snow cover. Although we addressed large-scale rectification errors by projecting images onto a digital elevation model to create orthomosaics, smaller discrepancies remain uncorrected. For instance, brightness differences due to surface tilt, oblique camera angles, and angular reflectivity can impact the variability in surface brightness. Further investigation of elevation differences across sea ice features could improve our understanding of these effects, especially for applications in the Antarctic, where the variability in snow thickness is greater than in the Arctic (Garnier et al., 2021) and the absence of melt ponds may introduce additional uncertainties into fixed-altitude remote sensing data.

5. Conclusion and outlooks

In this study, we have introduced a straightforward approach for delivering ice floe-scale estimates of solar radiative energy deposition from simple aerial imagery. We used surface brightness as a proxy for surface albedo, because such data, for example, recorded from drones or helicopters, are available from various field studies and will be even more common in future projects. Using composites of several photos, surface albedo can be mapped on scales of several hundreds of meters, revealing spatial differences and variability. This method contributes to bridging the gap in scaling in-situ observations to a larger scale, for example, to advancing measurements from autonomous stations and along survey lines to a larger area and across different surface types.

Based on this method, we quantified the seasonal evolution and spatial variability of surface brightness and energy deposition of Arctic sea ice during the melt and freeze-up seasons. The results show that grids of 200 m × 200 m and larger are needed for an adequate representation of spatial variability and thus of energy transfer into the ice-covered surface in summer. From this scale upward, sufficient parts of different surface features are included. Also, the mean surface brightness is within 10% of that of the entire ice floe. In contrast, over smaller areas, the difference in energy deposition can vary significantly between different sites. Energy budgets of melt ponds and bare ice surfaces may differ by more than 600%, when investigating an area length of 10 m, and over 300% for an area length of 100 m. These differences should be considered when deciding on observational strategies (i.e., the distribution of measurement time and resources) in future studies.

This study shows how spatial variability varies with seasonal surface evolution. Although developments were not linear or continuous, our results show that studies in the middle of melt seasons need to cover larger areas in order to capture the aspect of spatial variability. The scales of observation need to vary at different times, where a larger area is needed to capture full variability in the middle of the melt season, while a 200 m grid proves to be sufficient, as the mean surface brightness converges to the mean of the ice floe, even from melt onset to freeze onset of the sea ice surface. When the Arctic sea ice is transitioning from mid-melt season to freeze onset, the influence of melt ponds on the energy deposition decreased from 61% to less than 1% (after the freeze onset).

This study provides a comprehensive scheme to observe the sea ice surface energy deposition as a function of the sampling area. Future work should extend our understanding of the scales of spatial variability to under-ice light fields, thus to provide a pan-Arctic view to energy partitioning into and through sea ice. This extension would provide new information on the seasonal evolution of radiative portioning of different sea ice surface types both into and underneath the ice. The availability of two-dimensional surface fluxes would allow a full three-dimensional energy transfer analysis through sea ice based on observational data, leading to insights into lateral fluxes and more realistic energy/light distributions in and under sea ice, which are also crucial for ecological studies. This study paves the way to upscale the radiative partitioning to ice floe-scale, thus improving our understanding of the energy budget of the Arctic sea ice.

Data Accessibility Statement

The helicopter-borne RGB orthomosaics are available on Pangaea (Neckel et al., 2023, https://doi.org/10.1594/PANGAEA.949433). The MOSAiC radiation stations data are available on Pangaea (Tao et al., 2022, https://doi.pangaea.de/10.1594/PANGAEA.949556). Snow Buoys 2019S94 and 2020S106 are published on Pangaea (Nicolaus et al., 2020, https://doi.org/10.1594/PANGAEA.925325; Nicolaus et al., 2021, https://doi.org/10.1594/PANGAEA.937174). The in-situ albedo measurements are available via the National Science Foundation's Arctic Data Center (Smith et al., 2021a, doi:10.18739/A2KK94D36; Smith et al., 2021b, doi:10.18739/A2FT8DK8Z).

Acknowledgments

This work was carried out and data used in this manuscript were produced as part of the international Multidisciplinary drifting Observatory for the Study of the Arctic Climate (MOSAiC) with the tag MOSAiC20192020. We thank all persons involved in the expedition of the research vessel *Polarstern* during MOSAiC in 2019–2020 (AWI_PS122_00) as listed in Nixdorf et al. (2021).

Funding

This work was funded by the German Federal Ministry of Education and Research (BMBF) through financing the Alfred-Wegener-Institut Helmholtz-Zentrum für Polar- und Meeresforschung (AWI) and the *Polarstern* expedition PS122 under the grant N-2014-H-060_Dethloff to the AWI through its projects: AWI_ROV, AWI_ICE, and AWI_SNOW. The AWI buoy program was funded by the Helmholtz strategic investment Frontiers in Arctic Marine Monitoring (FRAM). Part of the funding for this project was provided by the Deutsche Forschungsgemeinschaft (DFG, German Research Foundation)—Project-ID 268020496—through the Transregional Collaborative Research Centre TRR-172 "ArctiC Amplification: Climate Relevant Atmospheric and SurfaCe Processes, and Feedback Mechanisms (AC)^3." RT was funded by the Deutsche Forschungsgemeinschaft (DFG, German Research Foundation)—Project-ID 268020496—through the Transregional Collaborative Research Centre TRR-172 "ArctiC Amplification: Climate Relevant Atmospheric and SurfaCe Processes, and Feedback Mechanisms (AC)^3." NF received funding from the German Ministry for Education and Research (BMBF) through the project NiceLABpro (grant no. 03F0867A) and funding from the Deutsche Forschungsgemeinschaft under Germany's Excellence Strategy (EXC 2037; CLICCS—Climate, Climatic Change, and Society; grant no. 390683824). MMS was funded by NSF OPP 2138787. BL was funded by NSF OPP-2138787 and OPP-2143547.

Competing interests

The authors declare that they have no conflict of interest.

Author contributions

RT generated the concept of this study to investigate the scales and impact of surface spatial variability at a larger range of the ice floe. RT and MN designed the study areas, analysis approach and conducted the data interpolation. Co-authors helped in formulating the discussion. NF, NN, and SG collected surface images. BL and MMS collected in-situ measurement. All authors provided input to the writing or revising of the manuscript and approved its submission.

References

Bliss, AC, **Anderson, MR.** 2018. Arctic sea ice melt onset timing from passive microwave-based and surface air temperature-based methods. *Journal of Geophysical Research: Atmospheres* **123**: 9063–9080. DOI: https://doi.org/10.1029/2018jd028676.

Boeke, RC, **Taylor, PC.** 2018. Seasonal energy exchange in sea ice retreat regions contributes to differences in projected Arctic warming. *Nature Communications* **9**: 5017. DOI: https://doi.org/10.1038/s41467-018-07061-9.

Calmer, R, **de Boer, G**, **Hamilton, J**, **Lawrence, D**, **Webster, MA**, **Wright, N**, **Shupe, MD**, **Cox, CJ**, **Cassano, JJ.** 2023. Relationships between summertime surface albedo and melt pond fraction in the central Arctic Ocean: The aggregate scale of albedo obtained on the MOSAiC floe. *Elementa Science of the Anthropocene* **11**(1): 00001. DOI: https://doi.org/10.1525/elementa.2023.00001.

Carlsen, T, **Birnbaum, G**, **Ehrlich, A**, **Helm, V**, **Jäkel, E**, **Schäfer, M**, **Wendisch, M.** 2020. Parameterizing anisotropic reflectance of snow surfaces from airborne digital camera observations in Antarctica. *The Cryosphere* **14**: 3959–3978. DOI: https://doi.org/10.5194/tc-14-3959-2020.

Cox, CJ, **Gallagher, MR**, **Shupe, MD**, **Persson, POG**, **Solomon, A**, **Fairall, CW**, **Ayers, T**, **Blomquist, B**, **Brooks, IM**, **Costa, D**, **Grachev, A**, **Gottas, D**, **Hutchings, JK**, **Kutchenreiter, M**, **Leach, J**, **Morris, SM**, **Morris, V**, **Osborn, J**, **Pezoa, S**, **Preußer, A**, **Riihimaki, LD**, **Uttal, T.** 2023. Continuous observations of the surface energy budget and meteorology over the Arctic sea ice during MOSAiC. *Scientific Data* **10**: 519. DOI: https://doi.org/10.1038/s41597-023-02415-5.

Curry, JA, **Schramm, JL**, **Ebert, EE.** 1995. Sea ice-albedo climate feedback mechanism. *Journal of Climate* **8**(2): 240–247.

Ehrlich, A, **Bierwirth, E**, **Wendisch, M**, **Herber, A**, **Gayet, J-F.** 2012. Airborne hyperspectral observations of surface and cloud directional reflectivity using a commercial digital camera. *Atmospheric Chemistry and Physics* **12**: 3493–3510. DOI: https://doi.org/10.5194/acp-12-3493-2012.

Fuchs, N. 2023. *A multidimensional analysis of sea ice melt pond properties from aerial images*. Universitaet Bremen. DOI: https://doi.org/10.26092/elib/2249.

Garnier, F, **Fleury, S**, **Garric, G**, **Bouffard, J**, **Tsamados, M**, **Laforge, A**, **Bocquet, M**, **Hansen, RMF**, **Remy, F.** 2021. Advances in altimetric snow depth estimates using bi-frequency SARAL and CryoSat-2 Ka–Ku measurements. *The Cryosphere* **15**: 5483–5512. DOI: https://doi.org/10.5194/tc-15-5483-2021.

Gómez-Hernández, J, **Sosres, A**, **Froidevaus, R** eds. 1999. GeoENV II—Geostatistics for environmental applications. In *Proceedings of the Second European Conference on Geostatistics for Environmental Applications held in Valencia, Spain, November 18–20, 1998*. Dordrecht, The Netherlands: Springer: 562. DOI: https://doi.org/10.1007/978-94-015-9297-0.

Grenfell, TC, **Maykut, GA.** 1977. The optical properties of ice and snow in the Arctic Basin. *Journal of Glaciology* **18**(80): 445–463. DOI: https://doi.org/10.3189/S0022143000021122.

Hudson, SR, **Granskog, MA**, **Sundfjord, A**, **Randelhoff, A**, **Renner, AHH**, **Divine, DV.** 2013. Energy budget of first-year Arctic sea ice in advanced stages of melt. *Geophysical Research Letters* **40**: 2679–2683. DOI: https://doi.org/10.1002/grl.50517.

Kashiwase, H, **Ohshima, KI**, **Nihashi, S**, **Eicken, H.** 2017. Evidence for ice-ocean albedo feedback in the Arctic Ocean shifting to a seasonal ice zone. *Scientific Reports* **7**: 8170. DOI: https://doi.org/10.1038/s41598-017-08467-z.

Katlein, C, **Arndt, S**, **Nicolaus, M**, **Perovich, DK**, **Jakuba, MV**, **Suman, S**, **Elliott, S**, **Whitcomb, LL**, **McFarland, CJ**, **Gerdes, R**, **Boetius, A**, **German, CR.** 2015. Influence of ice thickness and surface properties on light transmission through Arctic sea ice. *Journal of Geophysical Research: Oceans* **120**: 5932–5944. DOI: https://doi.org/10.1002/2015jc010914.

Knust, R. 2017. Polar Research and Supply Vessel POLARSTERN operated by the Alfred-Wegener-Institute. *Journal of Large-Scale Research Facilities* **3**. DOI: https://doi.org/10.17815/jlsrf-3-163.

Krumpen, T, **von Albedyll, L**, **Goessling, HF**, **Hendricks, S**, **Juhls, B**, **Spreen, G**, **Willmes, S**, **Belter, HJ**, **Dethloff, K**, **Haas, C**, **Kaleschke, L**, **Katlein, C**, **Tian-Kunze, X**, **Ricker, R**, **Rostosky, P**, **Rückert, J**, **Singha, S**, **Sokolova, J.** 2021. MOSAiC drift expedition from October 2019 to July 2020: Sea ice conditions from space and comparison with previous years. *The Cryosphere* **15**(8): 3897–3920. DOI: https://doi.org/10.5194/tc-15-3897-2021.

Lei, R, **Cheng, B**, **Hoppmann, M**, **Zhang, F**, **Zuo, G**, **Hutchings, JK**, **Lin, L**, **Lan, M**, **Wang, H**, **Regnery, J**, **Krumpen, T**, **Haapala, J**, **Rabe, B**, **Perovich, DK**, **Nicolaus, M.** 2022. Seasonality and timing of sea ice mass balance and heat fluxes in the Arctic transpolar drift during 2019–2020. *Elementa: Science of the Anthropocene* **10**(1). DOI: https://doi.org/10.1525/elementa.2021.000089.

Light, B, **Smith, MM**, **Perovich, DK**, **Webster, MA**, **Holland, MM**, **Linhardt, F**, **Raphael, IA**, **Clemens-Sewall, D**, **Macfarlane, AR**, **Anhaus, P**, **Bailey, DA.** 2022. Arctic sea ice albedo: Spectral composition, spatial heterogeneity, and temporal evolution observed during the MOSAiC drift. *Elementa: Science of the Anthropocene* **10**(1). DOI: https://doi.org/10.1525/elementa.2021.000103.

Macfarlane, AR, **Dadic, R**, **Smith, MM**, **Light, B**, **Nicolaus, M**, **Henna-Reetta, H**, **Webster, M**, **Linhardt, F**, **Hämmerle, S**, **Schneebeli, M.** 2023. Evolution of the microstructure and reflectance of the surface scattering layer on melting, level Arctic sea ice. *Elementa Science of the Anthropocene* **11**(1). DOI: https://doi.org/10.1525/elementa.2022.00103.

Meiners, KM, **Arndt, S**, **Bestley, S**, **Krumpen, T**, **Ricker, R**, **Milnes, M**, **Newbery, K**, **Freier, U**, **Jarman, S**, **King, R**, **Proud, R**, **Kawaguchi, S**, **Meyer, B.** 2017. Antarctic pack ice algal distribution: Floe-scale spatial variability and predictability from physical parameters. *Geophysical Research Letters* **44**: 7382–7390. DOI: https://doi.org/10.1002/2017gl074346.

Neckel, N, **Fuchs, N**, **Birnbaum, G**, **Hutter, N**, **Jutila, A**, **Buth, L**, **von Albedyll, L**, **Ricker, R**, **Haas, C.** 2023. Helicopter-borne RGB orthomosaics and photogrammetric digital elevation models from the MOSAiC Expedition. *Scientific Data* **10**: 426. DOI: https://doi.org/10.1038/s41597-023-02318-5.

Nicolaus, M, **Gerland, S**, **Hudson, SR**, **Hanson, S**, **Haapala, J**, **Perovich, DK.** 2010. Seasonality of spectral albedo and transmittance as observed in the Arctic Transpolar Drift in 2007. *Journal of Geophysical Research: Atmospheres* **115**(C11). DOI: https://doi.org/10.1029/2009jc006074.

Nicolaus, M, **Hoppmann, M**, **Lei, R**, **Belter, HJ**, **Fang, YC**, **Rohde, J.** 2020. Snow height on sea ice, meteorological conditions and drift of sea ice from autonomous measurements from buoy 2019S94, deployed during MOSAiC 2019/20. Alfred Wegener Institute, Helmholtz Centre for Polar and Marine Research. PANGAEA. DOI: https://doi.org/10.1594/PANGAEA.925325.

Nicolaus, M, **Hoppmann, M**, **Regnery, J.** 2021. Snow height on sea ice, meteorological conditions and drift of sea ice from autonomous measurements from buoy 2020S106, deployed during MOSAiC 2019/20. Alfred Wegener Institute, Helmholtz

Centre for Polar and Marine Research. PANGAEA. DOI: https://doi.org/10.1594/PANGAEA.937174.

Nicolaus, M, Perovich, DK, Spreen, G, Granskog, MA, on Albedyll, LV, Angelopoulos, M, Anhaus, P, Arndt, S, Belter, HJ, Bessonov, V, Birnbaum, G, Brauchle, J, Calmer, R, Cardellach, E, Cheng, B, Clemens-Sewall, D, Dadic, R, Damm, E, De Boer, G, Demir, O, Dethloff, K, Divine, DV, Fong, AA, Fons, S, Frey, MM, Fuchs, N, Gabarró, C, Gerland, S, Goessling, HF, Gradinger, R, Haapala, J, Haas, C, Hamilton, J, Hannula, H-R, Hendricks, S, Herber, A, Heuzé, C, Hoppmann, M, Høyland, KV, Huntemann, M, Hutchings, JK, Hwang, B, Itkin, P, Jacobi, H-W, Jaggi, M, Jutila, A, Kaleschke, L, Katlein, C, Kolabutin, N, Krampe, D, Kristensen, SS, Krumpen, T, Kurtz, N, Lampert, A, Lange, BA, Lei, R, Light, B, Linhardt, F, Liston, GE, Loose, B, Macfarlane, AR, Mahmud, M, Matero, IO, Maus, S, Morgenstern, A, Naderpour, R, Nandan, V, Niubom, A, Oggier, M, Oppelt, N, Pätzold, F, Perron, C, Petrovsky, T, Pirazzini, R, Polashenski, C, Rabe, B, Raphael, IA, Regnery, J, Rex, M, Ricker, R, Riemann-Campe, K, Rinke, A, Rohde, J, Salganik, E, Scharien, RK, Schiller, M, Schneebeli, M, Semmling, M, Shimanchuk, E, Shupe, MD, Smith, MM, Smolyanitsky, V, Sokolov, V, Stanton, T, Stroeve, J, Thielke, L, Timofeeva, A, Tonboe, RT, Tavri, A, Tsamados, M, Wagner, DN, Watkins, D, Webster, M, Wendisch, M. 2022. Overview of the MOSAiC expedition: Snow and sea ice. *Elementa: Science of the Anthropocene* **10**(1): 000046. DOI: https://doi.org/10.1525/elementa.2021.000046.

Nixdorf, U, Dethloff, K, Rex, M, Shupe, M, Sommerfeld, A, Perovich, D, Nicolaus, M, Heuze, C, Rabe, B, Loose, B, Damm, E, Gradinger, R, Fong, A, Maslowski, W, Rinke, A, Kwok, R, Spreen, G, Wendisch, M, Herber, A, Hirsekorn, M, Mohaupt, V, Frickenhaus, S, Immerz, A, Weiss-Tuider, K, König, B, Mengedoht, D, Regnery, J, Gerchow, P, Ransby, D, Krumpen, T, Morgenstern, A, Haas, C, Kanzow, T, Rack, FR, Saitzev, V, Sokolov, V, Makarov, A, Schwarze, S, Wunderlich, T, Wurr, K, Boetius, A. 2021. MOSAiC extended acknowledgement. Zenodo. DOI: https://doi.org/10.5281/zenodo.5179738.

Perovich, DK. 1996. *The optical properties of sea ice*. Monograph 96–1. Hanover, NH: Cold Regions Research & Engineering Laboratory.

Perovich, DK. 2005. On the aggregate-scale partitioning of solar radiation in Arctic sea ice during the Surface Heat Budget of the Arctic Ocean (SHEBA) field experiment. *Journal of Geophysical Research* **110**(C3). DOI: https://doi.org/10.1029/2004jc002512.

Perovich, DK, Andreas, EL, Curry, JA, Eiken, H, Fairall, CW, Grenfell, TC, Guest, PS, Intrieri, J, Kadko, D, Lindsay, RW, McPhee, MG, Morison, J, Moritz, RE, Paulson, CA, Pegau, WS, Persson, POG, Pinkel, R, Richter-Menge, JA, Stanton, T, Stern, H, Sturm, M, Tucker, WB III, Uttal, T. 1999. Year on ice gives climate insights. *Eos* **80**(41): 481–486. DOI: https://doi.org/10.1029/eo080i041p00481-01.

Perovich, DK, Grenfell, TC, Light, B, Hobbs, PV. 2002. Seasonal evolution of the albedo of multiyear Arctic sea ice. *Journal of Geophysical Research* **107**(C10): SHE 20-1-SHE 20-13. DOI: https://doi.org/10.1029/2000jc000438.

Perovich, DK, Polashenski, C. 2012. Albedo evolution of seasonal Arctic sea ice. *Geophysical Research Letters* **39**(8). DOI: https://doi.org/10.1029/2012gl051432.

Raphael, IA, Perovich, DK, Polashenski, CM, Clemens-Sewall, D, Itkin, P, Lei, R, Nicolaus, M, Regnery, J, Smith, MM, Webster, M, Jaggi, M. 2024. Sea ice mass balance during the MOSAiC drift experiment: Results from manual ice and snow thickness gauges. *Elementa Science of the Anthropocene* **12**(1): 00040. DOI: https://doi.org/10.1525/elementa.2023.00040.

Renner, AHH, Dumont, M, Beckers, J, Gerland, S, Haas, C. 2013. Improved characterisation of sea ice using simultaneous aerial photography and sea ice thickness measurements. *Cold Regions Science and Technology* **92**: 37–47. DOI: https://doi.org/10.1016/j.coldregions.2013.03.009.

Rex, M, Metfies, K. 2023. The Expedition PS122/5 of the Research Vessel POLARSTERN to the Arctic Ocean in 2020, in Bornemann, H, Amir Sawadkuhi, S eds., *Berichte zur Polar- und Meeresforschung = Reports on Polar and Marine Research*. Bremerhaven: Alfred-Wegener-Institut Helmholtz-Zentrum für Polar- und Meeresforschung.

Sankelo, P, Haapala, J, Heiler, I, Rinne, E. 2010. Melt pond formation and temporal evolution at the drifting station Tara during summer 2007. *Polar Research* **29**(3): 311–321. DOI: https://doi.org/10.1111/j.1751-8369.2010.00161.x.

Schwanghart, W. 2023. Experimental (Semi-) Variogram. MATLAB Central File Exchange. Available at https://www.mathworks.com/matlabcentral/fileexchange/20355-experimental-semi-variogram. Accessed October 20, 2023.

Serreze, MC, Stroeve, J. 2015. Arctic sea ice trends, variability and implications for seasonal ice forecasting. *Philosophical Transactions of the Royal Society A* **373**: 20140159. DOI: https://doi.org/10.1098/rsta.2014.0159.

Shupe, MD, Rex, M, Blomquist, B, Persson, POG, Schmale, J, Uttal, T, Althausen, D, Angot, H, Archer, S, Bariteau, L, Beck, I, Bilberry, J, Bucci, S, Buck, C, Boyer, M, Brasseur, Z, Brooks, IM, Calmer, R, Cassano, J, Castro, V, Chu, D, Costa, D, Cox, CJ, Creamean, J, Crewell, S, Dahlke, S, Damm, E, de Boer, G, Deckelmann, H, Dethloff, K, Dütsch, M, Ebell, K, Ehrlich, A, Ellis, J, Engelmann, R, Fong, AA, Frey, MM, Gallagher, MR, Ganzeveld, L, Gradinger, R, Graeser, J, Greenamyer, V, Griesche, H, Griffiths, S, Hamilton, J, Heinemann, G, Helmig, D, Herber, A, Heuzé, C, Hofer, J, Houchens, T, Howard, D, Inoue, J, Jacobi, H-W, Jaiser, R, Jokinen, T, Jourdan, O,

Jozef, G, King, W, Kirchgaessner, A, Klingebiel, M, Krassovski, M, Krumpen, T, Lampert, A, Landing, W, Laurila, T, Lawrence, D, Lonardi, M, Loose, B, Lüpkes, C, Maahn, M, Macke, A, Maslowski, W, Marsay, C, Maturilli, M, Mech, M, Morris, S, Moser, M, Nicolaus, M, Ortega, P, Osborn, J, Pätzold, F, Perovich, DK, Petäjä, T, Pilz, C, Pirazzini, R, Posman, K, Powers, H, Pratt, KA, Preußer, A, Quéléver, L, Radenz, M, Rabe, B, Rinke, A, Sachs, T, Schulz, A, Siebert, H, Silva, T, Solomon, A, Sommerfeld, A, Spreen, G, Stephens, M, Stohl, A, Svensson, G, Uin, J, Viegas, J, Voigt, C, von der Gathen, P, Wehner, B, Welker, JM, Wendisch, M, Werner, M, Xie, ZQ, Yue, F. 2022. Overview of the MOSAiC expedition: Atmosphere. *Elementa: Science of the Anthropocene* **10**(1): 00060. DOI: https://doi.org/10.1525/elementa.2021.00060.

Smith, M, Light, B, Perovich, D, Webster, M, Anhaus, P, Clemens-Sewall, D, Linhardt, F, Macfarlane, A, Raphael, I, Bozzato, D, Brasseur, Z, Dadic, R, Fons, S, Immerz, A, Hannula, H-R, Hutchings, J, Pätzold, F, Regnery, J, Pirazzini, R, Tavri, A. 2021a. Broadband albedo measurements of the sea ice surface during the Multidisciplinary drifting Observatory for the Study of Arctic Climate (MOSAiC) campaign in the Central Arctic Ocean, April–September, 2020. Arctic Data Center. DOI: https://doi.org/10.18739/A2KK94D36.

Smith, M, Light, B, Perovich, D, Webster, M, Anhaus, P, Clemens-Sewall, D, Linhardt, F, Macfarlane, A, Raphael, I, Bozzato, D, Brasseur, Z, Dadic, R, Fons, S, Immerz, A, Hannula, H-R, Hutchings, J, Pätzold, F, Regnery, J, Pirazzini, R, Tavri, A. 2021b. Spectral albedo measurements of the sea ice surface during the Multidisciplinary drifting Observatory for the Study of Arctic Climate (MOSAiC) campaign in the Central Arctic Ocean, April–September 2020. Arctic Data Center. DOI: https://doi.org/10.18739/A2FT8DK8Z.

Smith, MM, Light, B, Macfarlane, AR, Perovich, DK, Holland, MM, Shupe, MD. 2022. Sensitivity of the Arctic Sea ice cover to the summer surface scattering layer. *Geophysical Research Letters* **49**(9). DOI: https://doi.org/10.1029/2022gl098349.

Stroeve, J, Notz, D. 2018. Changing state of Arctic sea ice across all seasons. *Environmental Research Letters* **13**: 103001. DOI: https://doi.org/10.1088/1748-9326/aade56.

Tao, R, Anhaus, P, Arndt, S, Belter, HJ, Hoppmann, M, Katlein, C, Matero, I, Regnery, J, Rohde, J, Nicolaus, M. 2022. Spectral radiation fluxes, albedo and transmittance from autonomous measurements, deployed during MOSAiC 2019/20 [dataset]. Bremerhaven, Germany: Alfred Wegener Institute, Helmholtz Centre for Polar and Marine Research. PANGAEA. DOI: https://doi.pangaea.de/10.1594/PANGAEA.949556.

Tao, R, Nicolaus, M, Katlein, C, Anhaus, P, Hoppmann, M, Spreen, G, Niehaus, H, Jäkel, E, Wendisch, M, Haas, C. 2024. Seasonality of spectral radiative fluxes and optical properties of Arctic sea ice during the spring–summer transition. *Elementa: Science of the Anthropocene* **12**(1): 00130. https://online.ucpress.edu/elementa/article/12/1/00130/200662/Seasonality-of-spectral-radiative-fluxes-and.

Tschudi, MA, Curry, JA, Maslanik, JA. 2001. Airborne observations of summertime surface features and their effect on surface albedo during FIRE/SHEBA. *Journal of Geophysical Research Atmospheres* **106**(D14): 15335–15344. DOI: https://doi.org/10.1029/2000jd900275.

von Albedyll, L, Hendricks, S, Grodofzig, R, Krumpen, T, Arndt, S, Belter, HJ, Cheng, B, Birnbaum, G, Hoppmann, M, Hutchings, J, Itkin, P, Lei, R, Nicolaus, M, Ricker, R, Rohde, J, Suhrhoff, M, Timofeeva, A, Watkins, D, Webster, M, Haas, C. 2022. Thermodynamic and dynamic contributions to seasonal Arctic sea ice thickness distributions from airborne observations. *Elementa Science of the Anthropocene* **10**(1). DOI: https://doi.org/10.1525/elementa.2021.00074.

Wang, M, Su, J, Li, T, Wang, X, Ji, Q, Cao, Y, Lin, L, Liu, Y. 2018. Determination of Arctic melt pond fraction and sea ice roughness from Unmanned Aerial Vehicle (UAV) imagery. *Advances in Polar Science* **29**(3): 181–189. DOI: https://doi.org/10.13679/j.advps.2018.3.00181.

Webster, MA, Holland, M, Wright, NC, Hendricks, S, Hutter, N, Itkin, P, Light, B, Linhardt, F, Perovich, DK, Raphael, IA, Smith, MM, von Albedyll, L, Zhang, J. 2022. Spatiotemporal evolution of melt ponds on Arctic sea ice. *Elementa: Science of the Anthropocene* **10**(1): 000072. DOI: https://doi.org/10.1525/elementa.2021.000072.

Wendisch, M, Macke, A, Ehrlich, A, Lüpkes, C, Mech, M, Chechin, D, Dethloff, K, Barientos, C, Bozem, H, Brückner, M, Clemen, HC, Crewell, S, Donth, T, Dupuy, R, Dusny, C, Ebell, K, Egerer, U, Engelmann, R, Engler, C, Eppers, O, Gehrmann, M, Gong, X, Gottschalk, M, Gourbeyre, C, Griesche, H, Hartmann, J, Hartmann, M, Heinold, B, Herber, A, Herrmann, H, Heygster, G, Hoor, P, Jafariserajehlou, S, Jäkel, E, Järvinen, E, Jourdan, O, Kästner, U, Kecorius, S, Knudsen, EM, Köllner, F, Kretzschmar, J, Lelli, L, Leroy, D, Maturilli, M, Mei, L, Mertes, S, Mioche, G, Neuber, R, Nicolaus, M, Nomokonova, T, Notholt, J, Palm, M, van Pinxteren, M, Quaas, J, Richter, P, Ruiz-Donoso, E, Schäfer, M, Schmieder, K, Schnaiter, M, Schneider, J, Schwarzenböck, A, Seifert, P, Shupe, MD, Siebert, H, Spreen, G, Stapf, J, Stratmann, F, Vogl, T, Welti, A, Wex, H, Wiedensohler, A, Zanatta, M, Zeppenfeld, S. 2019. The Arctic Cloud Puzzle: Using ACLOUD/PASCAL multi-platform observations to unravel the role of clouds and aerosol particles in Arctic amplification. *Bulletin of the American Meteorological Society* **100**: 841–871. https://journals.ametsoc.org/doi/pdf/10.1175/BAMS-D-18-0072.1.

How to cite this article: Tao, R, Nicolaus, M, Katlein, C, Fuchs, N, Neckel, N, Buth, L, Smith, MM, Light, B, Graupner, S, Haas, C. 2025. Spatial variability in surface brightness and solar energy deposition of Arctic sea ice. *Elementa: Science of the Anthropocene* 13(1). DOI: https://doi.org/10.1525/elementa.2024.00084

Domain Editor-in-Chief: Jody W. Deming, University of Washington, Seattle, WA, USA

Associate Editor: Stephen F. Ackley, Department of Geological Sciences, University of Texas at San Antonio, TX, USA

Knowledge Domain: Ocean Science

Part of an Elementa Special Feature: The Multidisciplinary Drifting Observatory for the Study of Arctic Climate (MOSAiC)

Published: October 18, 2025 **Accepted:** August 12, 2025 **Submitted:** November 20, 2024

ELEMENTA
Science of the Anthropocene

Elem Sci Anth is a peer-reviewed open access
journal published by University of California Press.